Sensitivity Analysis of Sentinel-2 Imagery to Assess Urban Tree Functional Traits: A Physical Approach Based on Local Climate Zones

Théo Le Saint, Jean Nabucet, Sidonie Lefebvre, Jean-Philippe Gastellu-Etchegorry, Laurence Hubert-Moy, Karine Adeline

remote sensing

MDPI

Article

Sensitivity Analysis of Sentinel-2 Imagery to Assess Urban Tree Functional Traits: A Physical Approach Based on Local Climate Zones

Théo Le Saint [1,2,*], Jean Nabucet [1], Sidonie Lefebvre [3], Jean-Philippe Gastellu-Etchegorry [4], Laurence Hubert-Moy [1] and Karine Adeline [2]

[1] UMR 6554 CNRS, LETG, University of Rennes, Place du Recteur Henri Le Moal, 35000 Rennes, France; jean.nabucet@univ-rennes2.fr (J.N.); laurence.moy@univ-rennes2.fr (L.H.-M.)
[2] DOTA, ONERA, Université de Toulouse, 31055 Toulouse, France; karine.adeline@onera.fr
[3] DOTA, ONERA, Université Paris Saclay, 31055 Palaiseau, France; sidonie.lefebvre@onera.fr
[4] Centre d'Etudes Spatiales de la BIOsphère—UPS, CNES, CNRS, IRD, University of Toulouse, 31055 Toulouse, France; jean-philippe.gastellu@cesbio.cnes.fr
* Correspondence: theo.le-saint@univ-rennes2.fr

Abstract: Urban trees contribute to urban well-being but face challenging environments that can reduce their lifespan and increase young tree mortality. Although many studies have used remote sensing data to monitor the functional status of trees in rural areas, few have done so in urban areas to assess the health or estimate the biomass of large green areas. This study assessed the suitability of using Sentinel-2 images to characterize two urban tree functional traits—leaf chlorophyll content (Cab) and leaf area density (LAD)—in isolated trees and tree rows. Simulated Sentinel-2 images were generated using the DART radiative transfer model, considering 16 tree-endogenous and 14 tree-exogenous parameters, with 15 vegetation indices (VIs) analyzed. Sensitivity analysis was performed in four contrasting urban environments using local climate zone taxonomy. The accuracy of the simulated images was validated with real Sentinel-2 images, field measurements, and ancillary data collected for four tree species in Rennes, France. The results showed that the tree parameters significantly influenced Sentinel-2 spectral bands, with NGBDI and OSAVI VIs being most sensitive to Cab and LAD. The model showed high accuracy, with a mean RMSE of 0.016 for key spectral bands. The results also highlighted the importance of considering ancillary data to capture specific urban characteristics.

Keywords: remote sensing; radiative transfer modelling; DART; vegetation indices; 3D modelling

Citation: Le Saint, T.; Nabucet, J.; Lefebvre, S.; Gastellu-Etchegorry, J.-P.; Hubert-Moy, L.; Adeline, K. Sensitivity Analysis of Sentinel-2 Imagery to Assess Urban Tree Functional Traits: A Physical Approach Based on Local Climate Zones. *Remote Sens.* **2024**, *16*, 4402. https://doi.org/10.3390/rs16234402

Academic Editors: Mohamed El Mekawy and Ihab Hamzi Hijazi

Received: 6 September 2024
Revised: 18 November 2024
Accepted: 20 November 2024
Published: 25 November 2024

1. Introduction

In the context of climate change, urban trees lie at the heart of land-use planning policies [1] as they provide many vital ecosystem services [2], including temperature regulation through shading and evapotranspiration [3], carbon storage [4] and biodiversity preservation [5]. Thus, vegetation in urban areas has many benefits for human health and the living environment [6]. However, the urban environment can be unsuitable for the proper development of trees due to many stress factors [7], such as (i) the condition of tree stands, which experience both mechanical (e.g., soil compaction, increase in their artificial nature due to surrounding impervious materials) and chemical (e.g., soil contamination, lack of nutrients) disturbances, (ii) the short distance to human infrastructure (e.g., permanently shaded, limited growth potential), (iii) the atmosphere (e.g., temperature, gas and aerosol concentrations) and (iv) night light pollution. Thus, while urban trees contribute to urban well-being, they also have to cope with a highly constrained environment that decreases their well-being. Several studies have illustrated the large consequences of these stress factors: urban trees have a shorter mean lifespan than trees in rural areas [8], isolated

and tree rows experience more stress than park trees [9], and young trees have a higher mortality rate in cities [10].

In this context, the large-scale monitoring of the functional status of urban trees is a major challenge. Field inventories of urban trees are often performed with only a few trees and on a yearly or decennial basis, as they require large amounts of human resources and are often time-consuming. Conversely, remote sensing can provide information about urban vegetation at the city scale at high spatial and temporal resolutions. Over the past decade, satellite remote sensing has been increasingly used in urban environments for vegetation-related issues, mainly to map urban green spaces that cover large areas and classify the species in them, and to a lesser extent for change detection, biomass estimation or health assessment [11]. The main data sources used for urban tree characterization with remote sensing data are LiDAR data (40%), aerial photographs (37%), ground-based photographs and videos (39%), and satellite imagery (31%), suggesting that satellite imagery is used less than other data sources [12]. Studies focused on characterizing trees and their condition showed that a large spatial and temporal coverage, the fine scale of the objects studied, and a high level of characterization were difficult to combine. For example, a large number of phenological studies have used MODIS data to highlight the relationship between phenology, urbanization and climate change. Although urban vegetation conditions were monitored with a large spatial coverage on a daily basis, vegetation types or species could not be discriminated due to the low spatial resolution of MODIS (500 m) [13–16]. Few studies have investigated the functional status of urban trees to assess their health or estimate their biomass, focusing only on large green areas [17,18]. Studies based on aerial/UAV hyperspectral imagery have successfully estimated the LAI, chlorophyll content and health status of urban trees [19] and detected trees affected by pests in urban parks [20]. Research gaps remain for fine-scale tree characterization and the monitoring of vegetation's functional status in urban areas using open access and high-resolution data such as Sentinel-2 images. To our knowledge, only a few studies have considered the tree row scale and used Sentinel-2 to monitor annual and intra-annual phenology [21] or species-specific responses to drought [22].

However, many studies conducted outside urban areas have demonstrated that satellite remote sensing can be used to monitor the functional status of vegetation, including the key functional traits [23–26] that encompass a variety of physiological and morphological variables with specific absorption features in vegetation reflectance spectra.

At the leaf scale, chlorophyll (a and b, Cab) and carotenoid (Car) pigments are indicators of photosynthetic activity [27], biomass production [28] and leaf photoprotection [29]. As Cab pigments are more sensitive to changes in external conditions than Car pigments, the leaf chlorophyll content can be selected as a suitable indicator of environmental stress and changes in temperature and humidity, as well as pollutant concentrations in the air and soil [30]. Equivalent water thickness (EWT) and leaf mass area (LMA) are indicators of plant water stress [31] and biomass [32]. Whereas Cab and Car absorb mainly light in the visible domain (VIS: 0.4–0.7 µm) [33], EWT and LMA influence mainly the near-infrared (NIR: 0.7–1.4 µm) and short-wave infrared regions (SWIR: 1.4–2.5 µm) [33]. At the canopy scale, LAI can be used to identify tree phenological stages [34] and their photosynthetic potential [35] from the VIS to SWIR wavelengths (VSWIR; 0.4–2.5 µm), especially in the NIR. In this study, we did not consider LAI (m^2/m^2) but instead (leaf area density (LAD, m^2/m^3), because the latter is more suited to the tree scale than LAI [36].

These vegetation traits (i.e., Cab, Car, EWT, LMA and LAI) can be estimated using satellite hyperspectral data due to their high spectral richness in the VSWIR [37]. However, the spatial and temporal resolutions of the hyperspectral satellite data currently collected, such as EnMAP and PRISMA, are too coarse (30 m and 27–29 days at nadir, respectively) to study urban trees. Among the available multispectral high/very-high-spatial-resolution satellite data (e.g., WorldView, RapidEye, Pleiades, QuickBird, PlanetScope), freely available Sentinel-2 imagery has the advantage of having a high spatial resolution (10 m VIS/NIR and 20 m red-edge (RE: 0.67–0.76 µm)/SWIR), a large number of spectral bands (10 bands

at 10–20 m) and a temporal resolution adapted to monitoring the intra-annual dynamics of vegetation [38]. Cab and LAI have been successfully estimated using Sentinel-2 data in tropical forests [25,39], temperate forests [40] and cropland [41]. Specifically, VIs such as STVI [42] and CCII [43], calculated from the RE and NIR bands, were used to estimate Cab, and other VIs such as SELI have been adapted to Sentinel-2 spectral characteristics [44] to estimate LAI. A recent study developed EWT inversion models based on Sentinel-2 images of a mangrove forest [45]. In contrast, Sentinel-2 data cannot be used to estimate Car or LMA in forested areas due to having a spectral resolution coarser than that of hyperspectral data.

To our knowledge, no study has used Sentinel-2 imagery to identify the functional traits of urban trees, even for Cab or LAI, mainly due to its spatial resolution creating mixed pixels of vegetation and urban materials. The high spatial and volumetric heterogeneity of urban areas, due to the presence of buildings and associated shadows [46] and the high spectral diversity of material types and conditions [47,48], strongly influences electromagnetic interactions and the signal received by spaceborne sensors (i.e., attenuation due to multiple diffusion and absorption effects and amplification due to exacerbated directional effects). The top-of-canopy reflectance measured at the pixel scale is influenced by tree-endogenous parameters (e.g., structure, geometry, phenological stage, crown and leaf characteristics) and tree-exogenous parameters related to the urban context in which the tree is located (i.e., distance of the tree to the nearest building, solar angles, street orientation and surrounding materials). Several vegetation indices have been developed to address challenges in complex environments such as urban areas with significant atmospheric variations and heterogeneous surfaces (mixed pixels and diversity of optical properties of materials). For example, the atmospheric-resistant vegetation index (ARVI) was adapted from the NDVI by including the blue band to correct for atmospheric effects, particularly those due to aerosols and urban pollution [49]. The OSAVI was also adapted from the NDVI to reduce the influence of bare ground on vegetation measurements [50], which is essential in urban environments where vegetation is often sparse and the ground is composed of several types of mineral surfaces and vegetation understory.

In this context, the main objective of this study was to explore the suitability of using Sentinel-2 to assess the functional traits of urban trees, thus addressing the challenge of mixed pixels with an original approach combining LCZ modelling and the use of a 3D radiative transfer code able to disentangle both the spectral and spatial contributions of materials in urban scenes. We chose to perform a sensitivity analysis by means of Sentinel-2 image simulations and quantify the influence of tree-exogenous and tree-endogenous parameters on Sentinel-2 spectral bands and vegetation indices in four different urban contexts (i.e., for four LCZs) using Sobol' indices. Sensitivity analysis with radiative transfer modelling is a powerful tool that can determine whether remote sensing reflectance values are able to capture subtle spectral variations due to specific vegetation traits [51–54]. Subsequently, we evaluated the accuracy of the simulated images in comparison to the real Sentinel-2 images. The results will highlight which vegetation functional trait is accessible in which best conditions.

To simulate Sentinel-2 images, we used the DART radiative transfer model [55], which was developed at CESBIO (https://dart.omp.eu/# accessed on 1 September 2024) and validated through the RAdiation transfer Model Intercomparison initiative (RAMI) [56]. Many urban studies have used DART due to its ability to represent the complexity of a 3-dimensional (3D) space [57]. To model 3D scenes, we selected and adapted the taxonomy of local climate zones (LCZs) to encompass a wide variety of urban contexts [58]. This taxonomy, introduced in 2012, was originally focused on urban climates and heat islands, but is increasingly used as a reference framework for studying urban vegetation [59,60].

2. Materials and Methods

2.1. Methodological Framework

We assessed the suitability of Sentinel-2 to characterize the functional traits of urban trees using Sentinel-2 images simulated with DART based on two scenarios—isolated trees (SC1) and tree rows (SC2)—for four urban environments using LCZs (Figure 1).

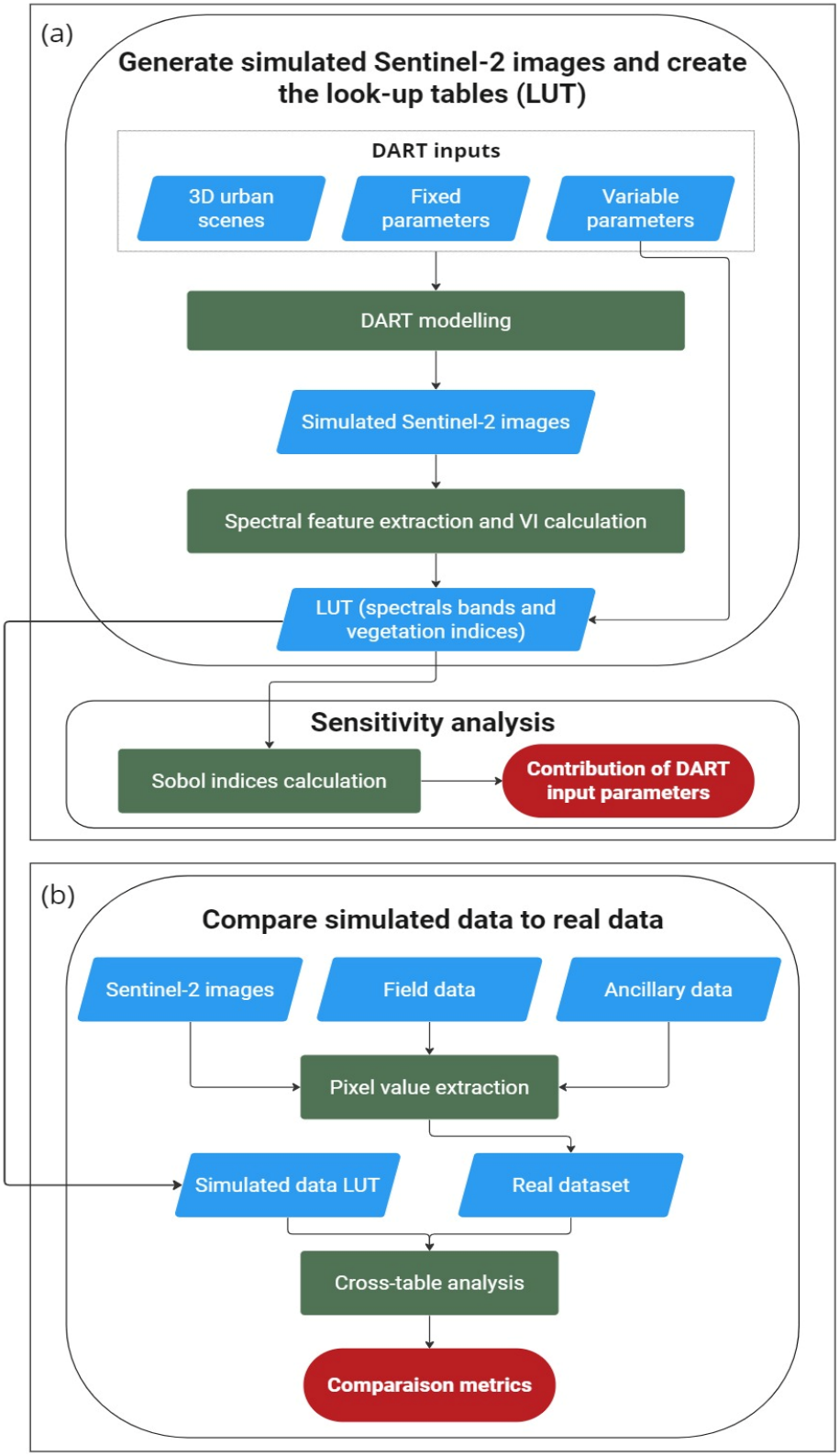

Figure 1. Workflow of the method. The method comprises two main steps: (**a**) generation of simulated Sentinel-2 images and creation of look-up tables, and (**b**) comparison of the simulated and real Sentinel-2 images.

The method consisted of two main steps. We first simulated Sentinel-2 images using DART and performed a sensitivity analysis of the look-up table (LUT) created from these simulated images for the two scenarios in the four LCZs. We then assessed the accuracy

with which the model simulated the real data based on five cloud-free real Sentinel-2 images and field measurements of Cab and LAD collected for four species in 2021 in Rennes, France.

Section 2.2 explains how the scenarios were defined and modelled with DART. The same workflow was applied to both scenarios to generate several simulated top-of-canopy reflectance Sentinel-2 images as a function of multiple parameters, including tree-endogenous parameters for tree functional traits and tree-exogenous parameters for tree environments.

Section 2.3 describes how the final LUT was created using the simulated images at a 1 m resolution according to the Sentinel-2 spectral characteristics and spatial windows with four configurations of mixed pixels according to the tree location (tree-centered and -shifted extracting windows) within the Sentinel-2 pixel at a 10 m resolution. The final LUT included DART input parameters, spectral bands and VIs selected for their sensitivity to the vegetation traits used for monitoring tree conditions.

Section 2.4 details the steps of the sensitivity analysis performed using Sobol' indices for both scenarios to assess the relative influence of selected parameters for tree functional traits and for environments on Sentinel-2-simulated spectral bands and VIs. Section 2.5 compares the simulated and real data based on a cross-table analysis.

2.2. Experimental Design for DART Modelling

2.2.1. Urban Scene and Tree Modelling Strategies

The 3D urban scenes that included trees were defined using the LCZ taxonomy. Four LCZ types were selected among the most dominant LCZ cover types encountered in European cities with more than 100,000 inhabitants (Figure 2): LCZ 2 (Compact Midrise), LCZ 5 (Open Midrise), LCZ 6 (Open Low-rise) and LCZ 8 (Large Low-rise).

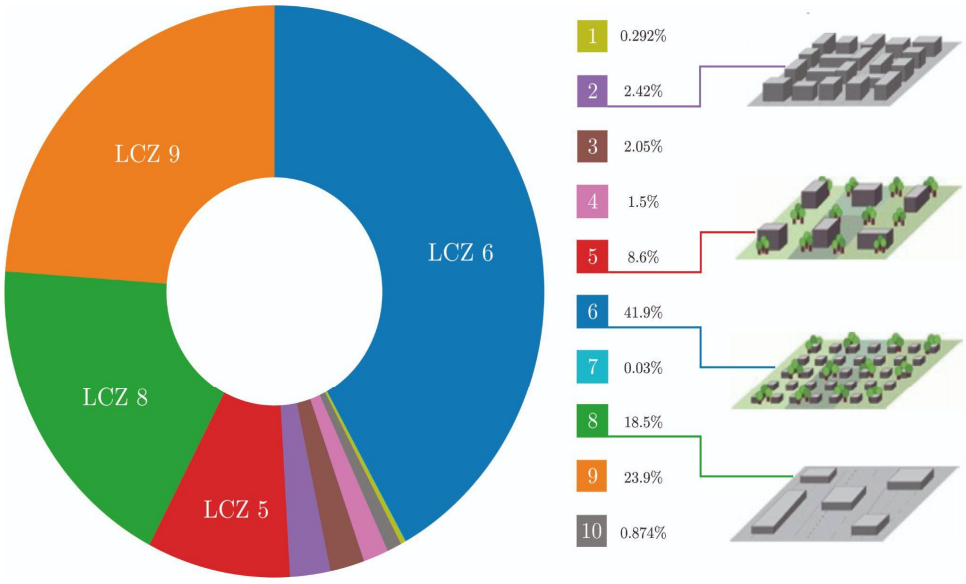

Figure 2. Distribution of local climate zones (LCZs) (as a percentage of surface area) in European Union cities with more than 100,000 inhabitants based on the European LCZ map [61] and administrative boundaries of the cities from EUROSTAT (© EuroGeographics © FAO (UN) © TurkStat). The thumbnails come from Stewart and Oke [58].

LCZ 9 (Sparsely built) describes areas with a low building density (15%), low height (6.5 m), and prevalence of pervious ground. Although this LCZ accounts for 24% of urban areas (Figure 2), it was discarded since its characteristics are very close to those of LCZ 6, which has a higher building density (30%). Given the Sentinel-2 spatial resolution, we preferentially selected LCZ 6 to better quantify the effects of an impervious ground type, shading and the proximity of trees to buildings on the reflectance values. Conversely, LCZ 2, which describes narrow urban canyons and accounts for 2.5% of urban areas

(Figure 2), was selected because this LCZ was very different from the other three selected LCZs. In this way, the four selected LCZs covered four contrasting environments, taking into account the diversity of urban landscapes and layouts.

Four LCZ parameters were used to build contrasting urban scenes (Table 1, Figure 3):

Table 1. Parameters used to generate mock-ups of the four local climate zones (LCZ).

Parameter	LCZ 2	LCZ 5	LCZ 6	LCZ 8
Height of roughness elements [m]	18	18	6.5	6.5
Aspect ratio	1.375	0.525	0.525	0.200
Building surface fraction [%]	55	30	30	40
Impervious ground surface fraction [%]	40	40	35	45
Pervious ground surface fraction [%]	5	30	35	15

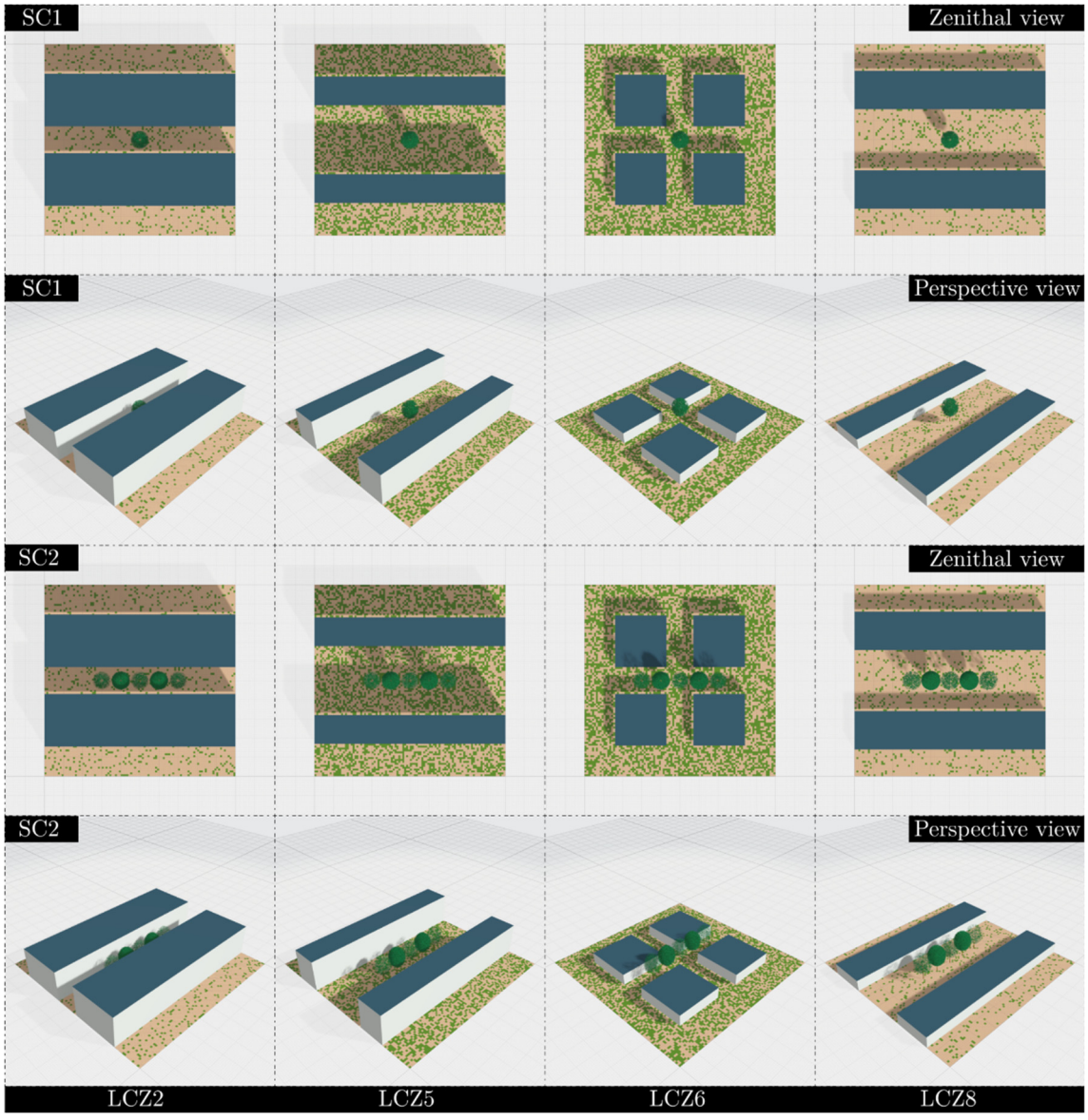

Figure 3. Three-dimensional urban scenes defined for the four local climate zones (LCZ) for scenarios SC1 (zenithal and perspective views) and SC2 (perspective view).

Height of roughness elements, which is the mean height of the buildings;

Aspect ratio, calculated as the height of roughness elements divided by the width of the urban canyon (street);

Building surface fraction, which is the percentage of the ground surface occupied by buildings;

Impervious ground surface fraction, which is the pervious ground surface fraction ratio.

We focused on deciduous trees, as they are found most often in major European cities, and specifically on isolated trees and tree rows, as they have been rarely studied using satellite remote sensing imagery. The tree modelling strategy was defined as follows:

Only deciduous tree species, which dominated the open access tree databases for eight European cities (i.e., Paris, Rennes, Toulouse, Lyon, Dublin, Amsterdam, Barcelona and Turin), were considered to limit the number of simulations;

The same reference tree was defined for both scenarios, in which certain structural dimensions were set to constants: tree height (15 m), crown height (11 m), crown diameter (10 m) and trunk diameter (0.4 m). These values were based on a statistical analysis of the tree row database of the Lyon metropolitan area, France (https://data.grandlyon.com/jeux-de-donnees/arbres-alignement-metropole-lyon/info, accessed on 1 September 2024). See Appendix A for details regarding the input tree characteristics. The reference tree was also modelled using an ellipsoid crown and a cylindrical trunk with branches, as in previous studies [62].

For SC2, rows of five trees were selected, and two profiles with specific tree functional traits were created to consider row heterogeneity. The central tree and the two trees at the ends of the row had the same first-profile characteristics for tree-endogenous parameters, while the other two trees had the same second profile (Figure 3).

The 3D mock-ups of the LCZs and tree morphologies were generated using an R code, and the final 3D objects created (.obj format) were used in DART.

2.2.2. DART Modelling

DART is a radiation transfer model that simulates canopy reflectance with light interactions and multiple scattering effects within a 3D scene, including the topography and atmosphere [57,63,64]. DART includes the model PROSPECT [65], which is used to model leaf reflectance and transmittance. We used DART version 5.8.10v1259.

Although DART includes many parameters to simulate Sentinel-2 images, we described 32 of them (Table 2 and Appendix A). These main parameters were tree-endogenous (11) or tree-exogenous (21), which have a direct or indirect effect on tree reflectance, respectively. While some parameters (16 for SC1 and 18 for SC2) were fixed, others (16 for SC1 and 14 for SC2) varied according to predefined values/ranges and distributions. We considered these variable parameters in the sensitivity analysis. The min and max bounds for the leaf traits were determined with reference to the literature to encompass a wide range of physiological statuses within the limitations of the PROSPECT model [66–68]. Given the wide range of urban materials and the variability in their optical properties, a selection was made among the most prevalent materials in European cities. These materials were assumed to have Lambertian spectral behavior as a first approximation [69], given the low spatial resolution of Sentinel-2.

A table of DART input parameters was created for the variable parameters (Table 2). Ultimately, 3000 simulations were performed per LCZ for both scenarios. Thus, 3000 points with coordinates [X1, . . ., Xp] were generated for each scenario, where p is the number of parameters, so that the experimental design covered the p-dimensional space as well as possible. The experimental design was performed using Latin hypercube sampling with the Python library OpenTurns [70].

Table 2. The main DART parameters used in this study by section of the DART graphical user interface, including their category (exogenous or endogenous), type ((F)ixed or (V)ariable for both scenarios, or V (SC1), which is variable for scenario SC1 and fixed for scenario SC2), value (if F) or range (if V), and SC1 and/or SC2 configuration.

DART Section	Parameter Name	Category	Type	Values and Range
Global settings	Light propagation mode	exogenous	F	Bi-directional (DART-Lux)
Sensor settings	Spectral bands	exogenous	F	According to Sentinel-2 sensor
	Zenithal angle	exogenous	F	2.8 [°]
	Azimuth angle	exogenous	F	182 [°]
	Spatial resolution	exogenous	F	1 [m]
Direction input parameter	Hour	exogenous	F	11:07 UTC
	Day	exogenous	F	Day 15 of each month
	Month	exogenous	V	From March to November
Atmosphere	Atmosphere model	exogenous	F	USSTD76
	Aerosol properties	exogenous	F	Urban Type Aerosol optical depth = 1
Scene optical properties	Reflection model	exogenous	F	Lambertian
	Roof	exogenous	V	See Appendix A
	Wall	exogenous	V	See Appendix A
	Impervious ground	exogenous	V	See Appendix A
	Pervious ground	exogenous	V	See Appendix A
Earth scene	Dimensions	exogenous	F	100 m × 100 [m]
	Latitude	exogenous	F	48.1°N
	Longitude	exogenous	F	1.68°W
	Temperature	Exogenous	F	300 [°K]
Tree planting conditions	Distance to nearest building	exogenous	V	LCZ2 and LCZ6: 5.0–6.5 [m] LCZ5 and LCZ8: 6–16 [m]
	Tree exposure	exogenous	V	Shady side or sunny side
	Street orientation [1]	exogenous	V	0, 45, 90 and 135 [°]
Tree	Geometric parameters	endogenous	F	See Table A1
	Leaf angle distribution (ldist)	endogenous	V	Plagiophile and planophile
	Leaf area density (LAD)	endogenous	V	0.1 and 1.2 [m^2/m^3]
Leaf	Clumping factor	endogenous	V (SC1)	0–50 [%]
	Structure coefficient (N)	endogenous	V	1.1–2.3 [arbitrary unit]
	Leaf chlorophylls content (Cab)	endogenous	V	5–60 [$\mu g/cm^2$]
	Carotenoid content (Car)	endogenous	V	2.5–25 [$\mu g/cm^2$]
	Brown pigment	endogenous	F	0 [arbitrary unit]
	Anthocyanin	endogenous	F	0 [$\mu g/cm^2$]
	Equivalent water thickness	endogenous	V (SC1)	0.004–0.024 [cm]
	Dry matter content	endogenous	V	0.002–0.014 [g/cm^2]

[1] The street orientation was set at an anti-clockwise angle: 0° = west/east, 45° = south-west/north-east, 90° = north/south and 135° = south-east/north-west.

The DART outputs were 100 × 100 pixel images. They were configured to match Sentinel-2's spectral and geometric (view angles) characteristics. Only the 10 m (VIS and PIR) and 20 m (RE and SWIR) bands were simulated. Central wavelengths and bandwidths were defined according to the characteristics of the MSI sensor. The zenithal and azimuthal angles were set to the mean Sentinel-2 view angles: 3° (with zenith = 0°) and 180° (with north = 0°), respectively. Sentinel-2 images were first simulated at a 1 m resolution and then aggregated at 10 and 20 m.

2.3. Generating LUT from Simulated Sentinel-2 Images

2.3.1. Extracting Spectral Features

We extracted spectral features per pixel using four pairs of extraction windows of 10 × 10 (Figure 4) and 20 × 20 m, each resolution with one tree-centred window for SC1 and SC2, and three windows shifted by 5 m at 0°, 45° or 90°, respectively, relative to the centre of the tree canopy in the direction of the tree row for SC2. The 20 × 20 m windows were configured so that their lower left quarter was the 10 × 10 m window.

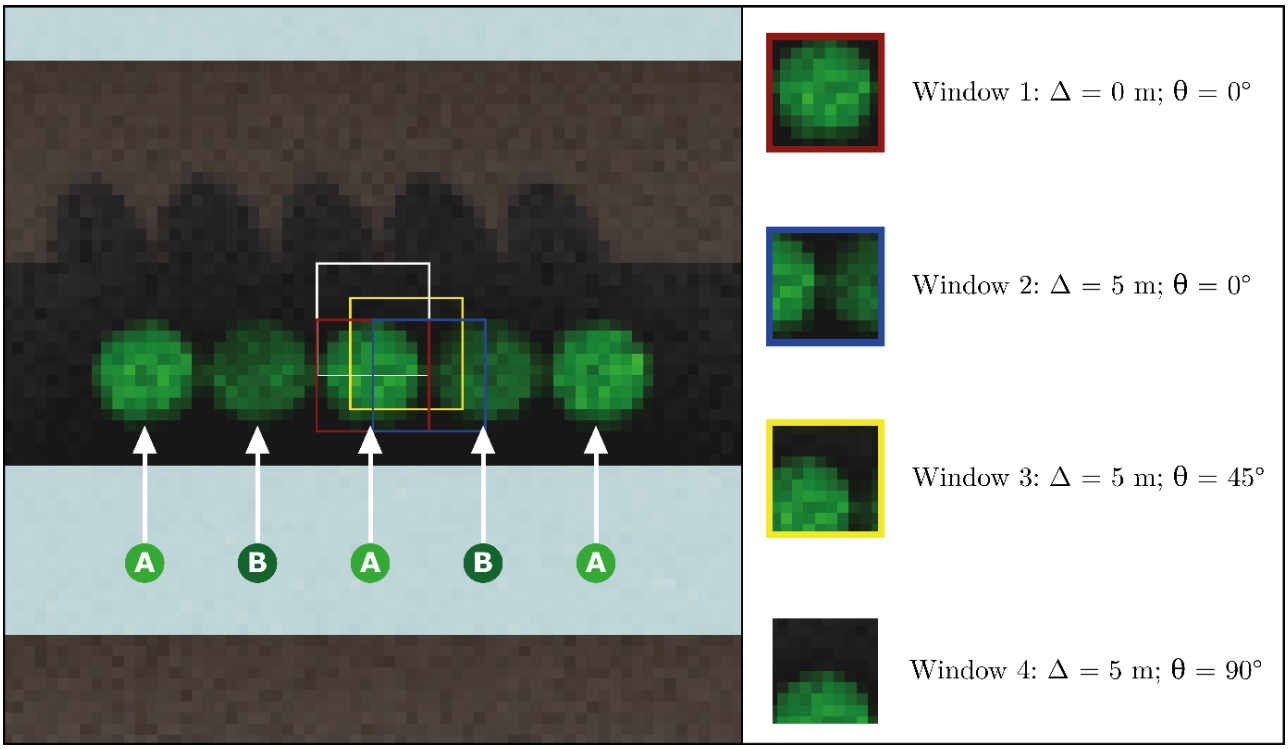

Figure 4. Examples of the four windows used to extract spectral features at a 10 m resolution. Delta (Δ) equals the offset between the window's centre and the tree's centroid, and theta (θ) equals the offset angle between the window's centre and the row axis relative to the tree's centroid. The central tree and the two trees at the ends of the row had the same first-profile characteristics for tree-endogenous parameters (A), while the other two trees had the same second profile (B).

We used the extraction window method to consider the heterogeneity (mixed pixels of vegetation and urban materials) and geolocation uncertainty of Sentinel-2 pixels. As each tree was randomly located within each pixel, the probability of having pure vegetation pixels was low. Moreover, the Sentinel-2 absolute geolocation error was assumed to be less than 6 m, and the co-registration error over several dates was assumed to be less than 5 m with 95% confidence [71]. In addition, two tree profiles can be considered using this window approach: the target tree profile (A) and the neighbour tree profile (B).

The pixel values of the simulated images were then extracted for each pair window area and averaged. A LUT was created with DART input parameters and S2 spectral features for the four window types, four LCZs and two scenarios.

2.3.2. Vegetation Indices Calculation

Three categories of VIs were calculated from the LUTs: simple, normalised or complex. Based on the literature, we selected VIs that had the strongest correlations with the LAI and chlorophyll content (Table 3).

Table 3. The vegetation indices used in this study, which were calculated from visible bands only (VIS) or all bands (multispectral (MS)).

Category	Name	Equation (with Band Names)	Band	Spatial Resolution	Reference
Simple	Difference vegetation index	$DVI = \frac{B08}{B04}$	MS	10 m	[72]
Normalized	Green Leaf Index	$GLI = \frac{2\times B03 - B04 - B02}{2\times B03 + B04 + B02}$	VIS	10 m	[73]
	Normalized green–blue difference index	$NGBDI = \frac{B03 - B02}{B03 + B02}$	VIS	10 m	[74]
	Normalized green–red difference index	$NGRDI = \frac{B03 - B04}{B03 + B04}$	VIS	10 m	[75]
	Red–Green–Blue vegetation Index	$RGBVI = \frac{B03^2 - (B02\times B04)}{B03^2 + (B02\times B04)}$	VIS	10 m	[76]
	Atmospheric resistant vegetation index	$ARVI = \frac{(B08 - (B04 - 1\times(B02 - B04)))}{(B08 + (B04 - 1\times(B02 - B04)))}$	MS	10 m	[49]
	Normalized Vegetation Index	$NDVI = \frac{B08 - B04}{B08 + B04}$	MS	10 m	[77]
	Red-edge NDVI	$NDVIRE = \frac{B08 - B05}{B08 + B05}$	MS	20 m	[78]
	Sentinel-2 LAI Index	$SELI = \frac{B8A - B05}{B8A + B05}$	MS	20 m	[44]
Complex	Sentinel-2 Triangular vegetation index	STVI (See reference)	MS	20 m	[42]
	Modified Chlorophyll Absorption in Reflectance Index 2	MCARI2 (See reference)	MS	10 m	[79]
	Transformed Chlorophyll Absorption Reflectance Index	$TCARI = 3\times[(B05 - B04) - 0.2\times(B05 - B03)\times(B05/B04)]$	MS	20 m	[80]
	Optimized Soil-Adjusted vegetation index	$OSAVI = (1 + 0.16)\times(B08 - B04)/(B08 + B04 + 0.16)$	MS	10 m	[50]
	Canopy chlorophyll inversion index	$CCII = \frac{TCARI}{OSAVI}$	MS	20 m	[80,81]

2.4. Sensitivity Analysis

We performed sensitivity analysis using Sobol' indices (SIs) to assess the sensitivity of the DART outputs (i.e., spectral bands and VIs) to changes in the input parameters (Table 2). The Sobol' method is a global sensitivity analysis based on functional variance decomposition that produces sensitivity indices and measures the relative influence of each parameter. Unlike other types of sensitivity indices, such as the Hilbert–Schmidt independence criterion or Fourrier or Morris indices, SIs can measure the effects of interactions between input parameters [82], which are large when the latter are interdependent. This was the case for three parameters in the present study—orientation, distance to the nearest building and exposure—which influence the percentage of shadow in the pixel.

Sobol' indices are estimated using a large number of simulations. In this study, the number of simulations was limited, as they were performed using a complex physical model (DART). Thus, it was necessary to first create metamodels to calculate the SIs. We used Gaussian process regression to create several multivariate metamodels based on a Matern 5/2 kernel. One metamodel was created from the input parameters for each output parameter (i.e., spectral band or VI), and the metamodel performances were assessed using a 70–30% training–testing split of the data and the Q^2 metric. All metamodels having $Q^2 > 0.9$ [83] SIs were calculated using Saltelli's algorithm [84] with the Python library OpenTurns [70].

2.5. Comparing Simulated and Real Data

We created a real dataset from S2 images, field data and ancillary data for four study sites.

2.5.1. Real Dataset

The four study sites were located in Rennes, in north-western France (48.1°N, 1.68°W) (Figure 5). Rennes is a medium-sized city of 222,485 inhabitants, with a population density of 4414 people/km^2 [85] and an oceanic climate. Each site corresponded to a mono-species tree row.

The real dataset included five cloudless Sentinel-2 images (tile T30UWU) that were acquired on the dates closest to the field measurement dates and downloaded from the THEIA platform (https://catalogue.theia-land.fr, accessed on 1 September 2024). Because field measurements were performed on 2 and 23 June, 21 July, 16 August and 2 September 2021, Sentinel-2 images were acquired for 5 and 15 June, 20 July, 14 August and 5 September 2021. The mean interval between the date of Sentinel-2 image acquisition and field measurements was 3.6 days. We co-registered the Sentinel-2 images with sub-pixel accuracy using a reference image with the Python library Arosics [86]. The Sentinel-2 reference image was georeferenced using visually identified control points on the orthophotograph of the Rennes metropolitan area in 2021. We then calculated VIs. Seven field campaigns were performed during the 2021 growing season. A total of 117 trees were monitored in four tree rows composed of the following deciduous species: *Platanus acerifolia* (PL) (29 trees), *Acer platanoides* (AC) (29 trees), *Quercus rubra* (QR) (30 trees) and *Fraxinus excelsior* (FR) (29 trees) (Figure 5). For each tree, leaf Cab was measured using a leaf clip (FORCE A, Dualex, Orsay, France). LAD was measured using a canopy analyzer (LAI-2200, LiCor, Lincoln, NE, USA), based on [87]; for each tree in the 4 cardinal directions, the 4 LAD values were then summed to obtain one value per tree, for each date. Data are available at https://zenodo.org/records/12751353 (accessed on 1 September 2024) and the measurement protocols for Cab and LAD values are explained in [88]. The real dataset included the following ancillary data (spatial vector layers):

Building extent (source: Etalab land registry, Direction générale des finances publiques, 2021);

Tree crown delineation (with tree crowns delimited manually using an orthophotograph of the Rennes metropolitan area in 2021);

Street linearization (key 'highways' and 'primary' and 'secondary' values were selected using OpenStreetMap [89].

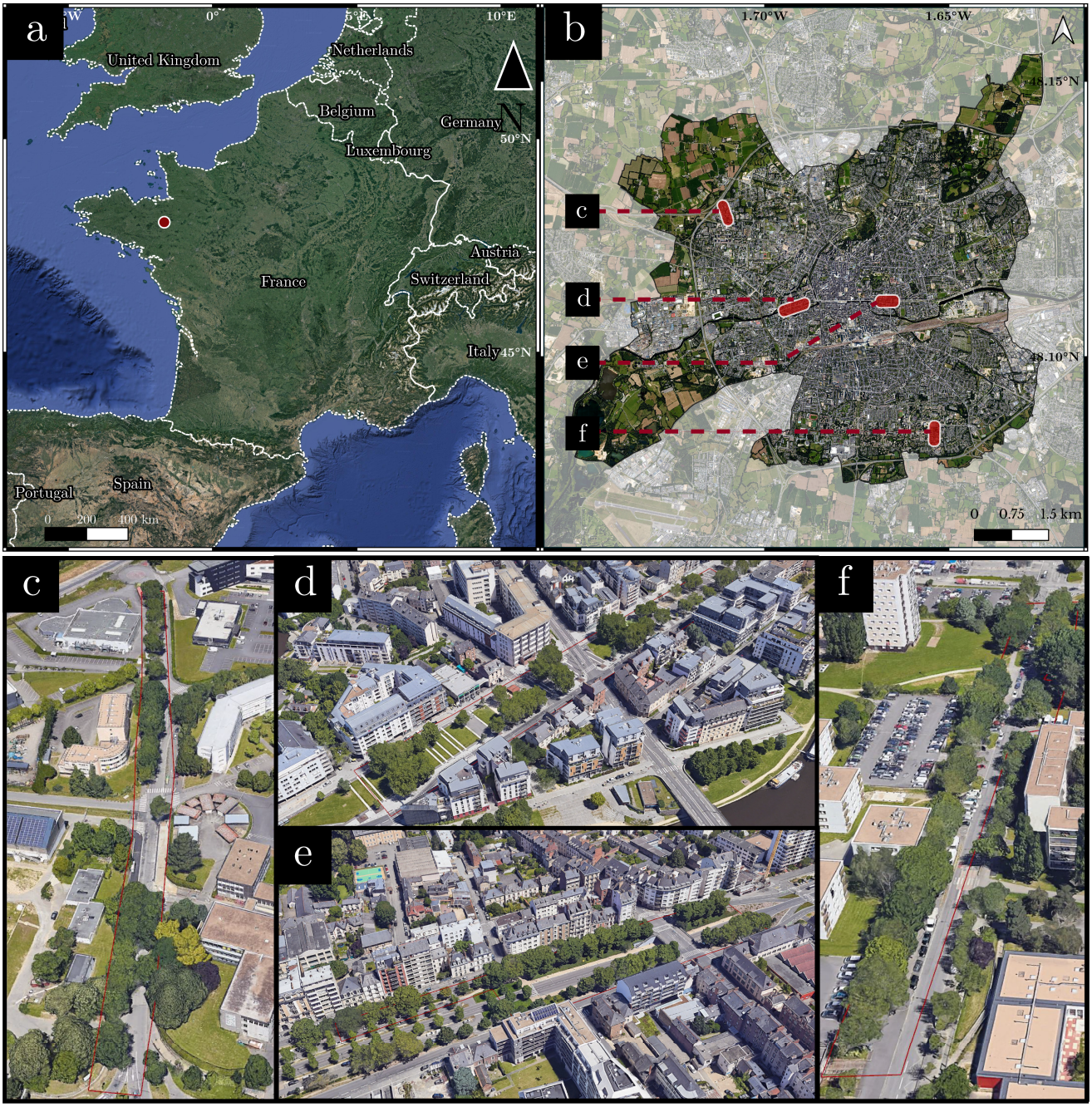

Figure 5. Location of the study sites. (**a**) Location of Rennes in France; (**b**) location of the four sites in Rennes; and sites of (**c**) Quercus rubra (QR), (**d**) Platanus acerifolia (PL), (**e**) Acer platanoides (AC) and (**f**) Fraxinus excelsior (FR). All photographs come from Google Maps 2021 3D view, except for (**b**) (2021 orthophotograph of the Rennes metropolitan area).

2.5.2. Extracting Pixel Values

A spatial reference grid corresponding to the Sentinel-2 matrix at a 10 m resolution (S2grid) and the tree crown delineation layer were used to classify the Sentinel-2 images. This spatial intersection yielded the number of trees, the identifier(s) of these trees and the percentage of the area occupied by each tree in each pixel.

One of the four window types was then assigned to each pixel based on the number of trees and the theoretical distribution of the canopy cover in the four windows (Table 4), as follows:

Table 4. Theoretical distribution of the percentages of canopy cover between trees A and B (Figure 6) in the four window types.

Window Type	Tree A	Tree B	Total	No. of Trees
1	78.0%	-	78%	1
2	39.0%	39.0%	78%	2
3	49.5%	18.0%	67.5%	2
4	39.0%	-	39%	1

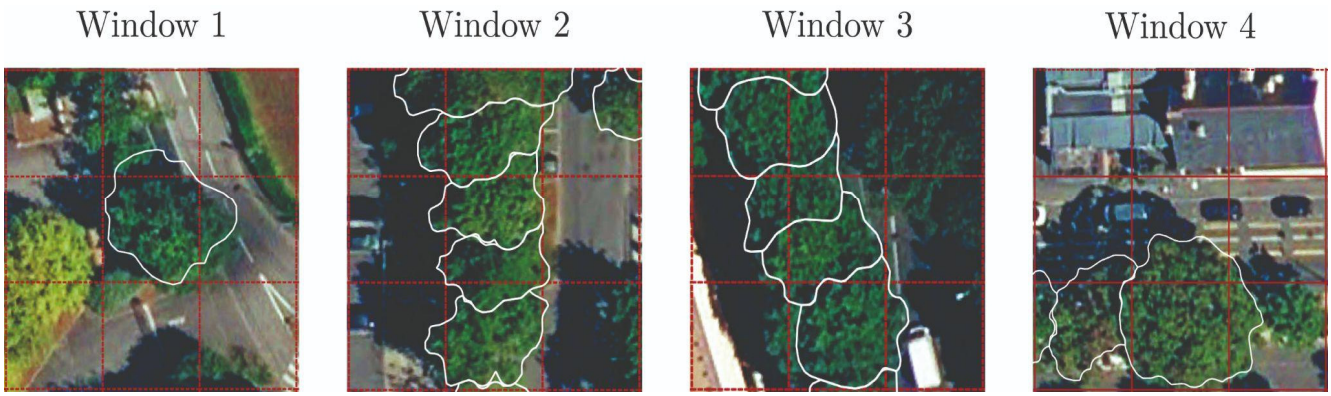

Figure 6. Examples of the four window types under real conditions. The white lines correspond to crown delineation, the red dotted grid corresponds to the Sentinel-2 grid at a 10 m resolution, and the central pixel of each thumbnail is the one classified. Images come from an orthophotograph of the Rennes metropolitan area in 2021.

When the pixel contained a single tree, we set a threshold of 58.5% canopy cover, which was the mean canopy cover of windows 1 (78%) and 4 (39%). When more than 58.5% of the pixel was covered, window 1 was assigned; if not, window 4 was assigned;

When the pixel contained two trees, the percentage of each tree in the total tree area in the pixel was calculated. When it was similar for both trees (40–60%), window 2 was assigned. When it differed (one < 40% and the other > 60%), window 3 was assigned.

We extracted 150 pixels that covered the 117 trees selected, as some of the trees were covered by several pixels. These pixels were classified by the type of window they had been assigned (Figure 6): 39 to window 1 (26%), 3 to window 2 (2%), 22 to window 3 (15%) and 86 to window 4 (57%).

Street orientation was calculated using the 'street linearization' layer, and the street angles were reclassified to the closest value of the LUT orientation parameter (i.e., 0°, 45°, 90° or 135°). The distance of trees to the nearest building was calculated from the centroid of each pixel to the nearest building using the 'building extent' layer. Exposure was calculated in several steps:

Identify the street segment (SA) nearest to each pixel centroid (P);

Calculate the line perpendicular (L) to SA that passes through P;

Define two intersection points (IP1 and IP2) between L and the building limits on both sides of the street;

Calculate the distance between P and IP1, and P and IP2;

Compare these distances according to street orientation and the solar azimuthal angle to determine whether the point lies on the sunny or shady side of the street. For example, in the case of a west–east street orientation, when the P-IP1 distance is superior to the P-IP2 distance, P is closer to the north building, which is on the sunny side of the street.

2.5.3. Cross-Table Analysis

A new LUT (S2LUT) based on real data was generated from the field data, ancillary data and Sentinel-2 images. To compare S2LUT and the simulated LUTs for SC2, all SC2

LUTs were merged into a single LUT (DARTLUT). S2LUT and DARTLUT were compared using the parameters common to both:

two continuous quantitative parameters: *Cab* and *LAD* (θ^1 and θ^2, respectively);

six qualitative or discrete quantitative parameters: LCZ type (i.e., 2, 5, 6 or 8), window type (i.e., 1–4), street orientation (i.e., 0°, 45°, 90° or 135°), tree-building distance (i.e., 6, 8, 10, 12, 14 or 16 m), exposure (sunny side or shady side) and date (month 3–10) (set as θ^3, θ^4, θ^5, θ^6, θ^7 and θ^8, respectively).

Specifically, for each S2LUT entity, we searched DARTLUT for all parameters in common. For quantitative parameters, we applied a search tolerance of ± 2 $\mu g/cm^2$ for Cab and ± 0.1 m^2/m^3 for LAD, whereas for qualitative parameters, we sought exact values. This filtering yielded DART VI and reflectance values to compare to corresponding S2 VI and reflectance values. We then used two matching methods to compare the reflectance and VIs simulated by DART to those obtained using S2 images: this resulted in the median of the 10% or 50% closest values. The root-mean-square error (*RMSE*) and the Pearson correlation coefficient (*r*) were used to compare the VI values. *RMSE* and *r* were computed according, respectively, to Equations (1) and (2), where V_{S2} corresponds to the value of the reflectance or VI in the S2LUT, V_{DART} corresponds to the value of the reflectance or VI in the DARTLUT, and n corresponds to the number of pixels in the S2LUT and matched DARTLUT pixels.

$$RMSE(V_{S2}, V_{DART}) = \sqrt{\frac{1}{n}\sum_{i=1}^{n}(V_{DARTi} - V_{S2i})^2} \quad (1)$$

$$r(V_{S2}, V_{DART}) = \frac{\sum_{i=1}^{n}\left(V_{S2i} - \overline{V_{S2}}\right) \times \left(V_{DARTi} - \overline{V_{DART}}\right)}{\sqrt{\sum_{i=1}^{n}\left(V_{S2i} - \overline{V_{S2}}\right)^2 \times \sum_{i=1}^{n}\left(V_{DARTi} - \overline{V_{DART}}\right)^2}} \quad (2)$$

3. Results

3.1. Sensitivity Analysis of the Simulated Isolated-Tree Scenario (SC1)

3.1.1. Spectral Bands

The sensitivity analysis of scenario SC1 revealed the strong influence of the tree-exogenous parameters in all LCZs on the Sentinel-2 spectral bands at a 20 m resolution, whereas the tree-endogenous parameters had nearly no influence (mean relative influence < 1%) regardless of the spectral band (Figure 7). However, the relative influences and spectral distributions of tree-exogenous parameters varied among the LCZs. Considering the tree-exogenous material parameters, roof materials had a larger influence when the street was narrow, as in LCZ2 (ca. 70–75%), whereas their influence decreased and that of ground materials (both impervious and pervious) increased in LCZs that were more open and had larger streets (LCZ2 > LCZ6 > LCZ5/LCZ8). Roof and ground materials remained those with the largest influences at a 20 m resolution. Pervious materials (i.e., grass) had nearly no influence in LCZ2 and LCZ8, but did in LCZ5 and LCZ6, especially on band B05 (relative influence of 25% and 50%, respectively). Regarding the tree-exogenous context parameters, the simulated Sentinel-2 reflectance was more sensitive to them in LCZ5, especially to exposure, which sometimes exceeded 25% for B8A, street orientation, which sometimes reached 18% for B11 and B12, and sun angles, which ranged from 5 to 10% among the spectral bands. The same results were observed in LCZ6 and LCZ8, but with smaller relative influences. The relative influence of street orientation was relatively large in all LCZs, especially LCZ2 and LCZ5. The distance to the nearest building had little influence, from 0% in LCZ2 to 3–4% in LCZ5, depending on the spectral band.

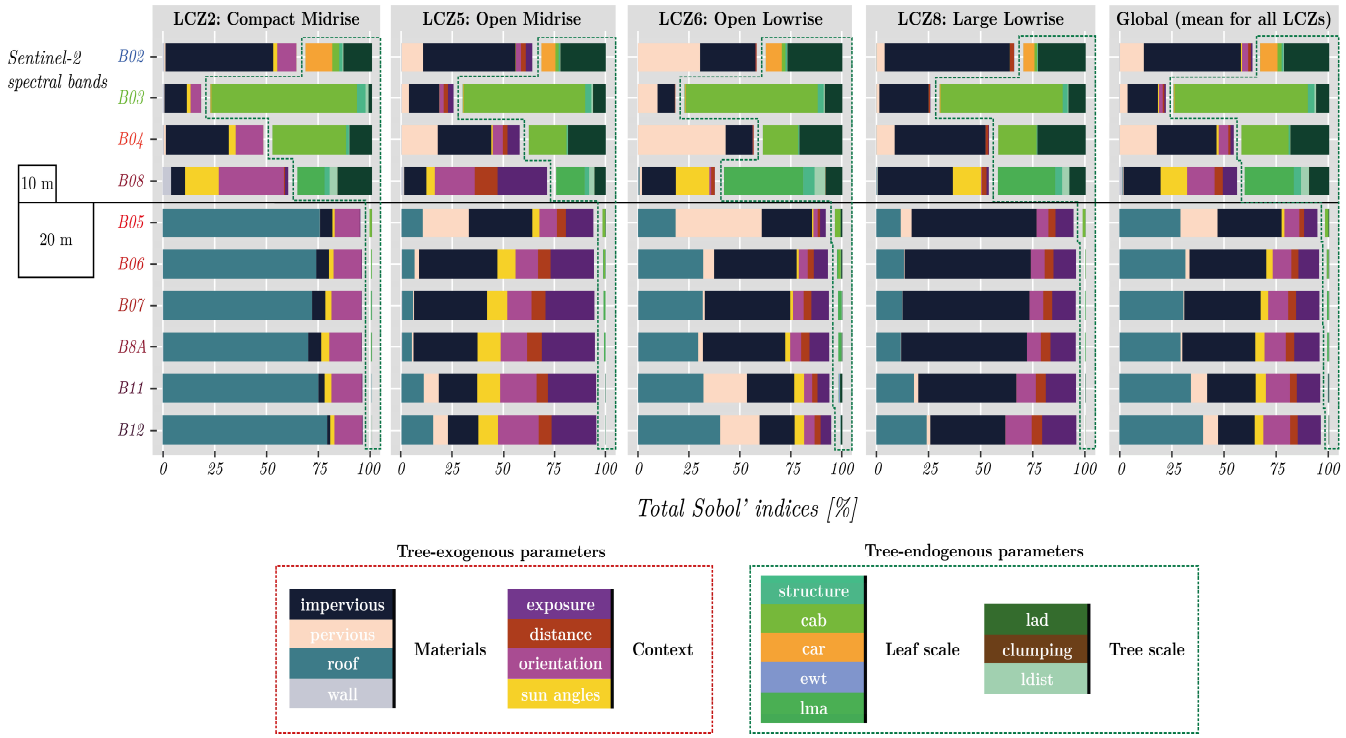

Figure 7. Sobol' indices for SC1 as a function of the local climate zone (LCZ) and spectral band, as well as in all LCZs combined.

In addition, the mean relative influence of tree-endogenous parameters on the S2 spectral bands at a 10 m resolution in all LCZs was much greater than those of the spectral bands at a 20 m resolution (34%, 77%, 43% and 42% on B02, B03, B04 and B08, respectively) (Figure 7). The tree-endogenous parameters that influenced B02 were mainly Car and LAD (mean of 9% and 22%, respectively). B03 was the spectral band influenced most by Cab, which had a relative influence of 73%, 62%, 68% and 61% in LCZ2, LCZ5, LCZ6 and LCZ8, respectively. B04 was influenced by both Cab and LAD. The relative influence of *LAD* varied among the LCZs, ranging from 18% in LCZ6 to 37% in LCZ2. LMA influenced B08 in LCZ6 and LCZ8 (40% and 28%, respectively). However, tree-exogenous parameters also influenced the reflectance. Ground materials strongly influenced the reflectance of B02-B04, while roof materials did not influence it. More diverse influences were observed for B08, with sun angles having a larger influence (i.e., 6.5–15.0% among the LCZs) and smaller influence than the other context parameters, depending on the LCZ. Regardless of the resolution or LCZ, wall materials had a negligible influence among the tree-exogenous parameters, as did clumping, LAD, structure and EWT among the tree-endogenous parameters. Overall, only LAD and Cab had a relative influence on reflectance greater than 20% for at least two spectral bands. To a lesser extent, Car and LMA influenced one spectral band each—B02 and B08, respectively—with a mean relative influence of less than 8.5% and 20%, respectively.

3.1.2. Vegetation Indices

The sensitivity analysis of scenario SC1 also revealed that the VIs were more sensitive to tree-endogenous parameters than the spectral bands were, and more so at 10 m (relative influences of 55–75%) than at 20 m (10–40%) (Figure 8). The two VIs with the largest tree-endogenous influences were NGBDI and OSAVI at 10 m, and CCII and TCARI at 20 m, while the VIs with the smallest influences were DVI and NGRDI at 10 m, and NDVIRE and SELI at 20 m.

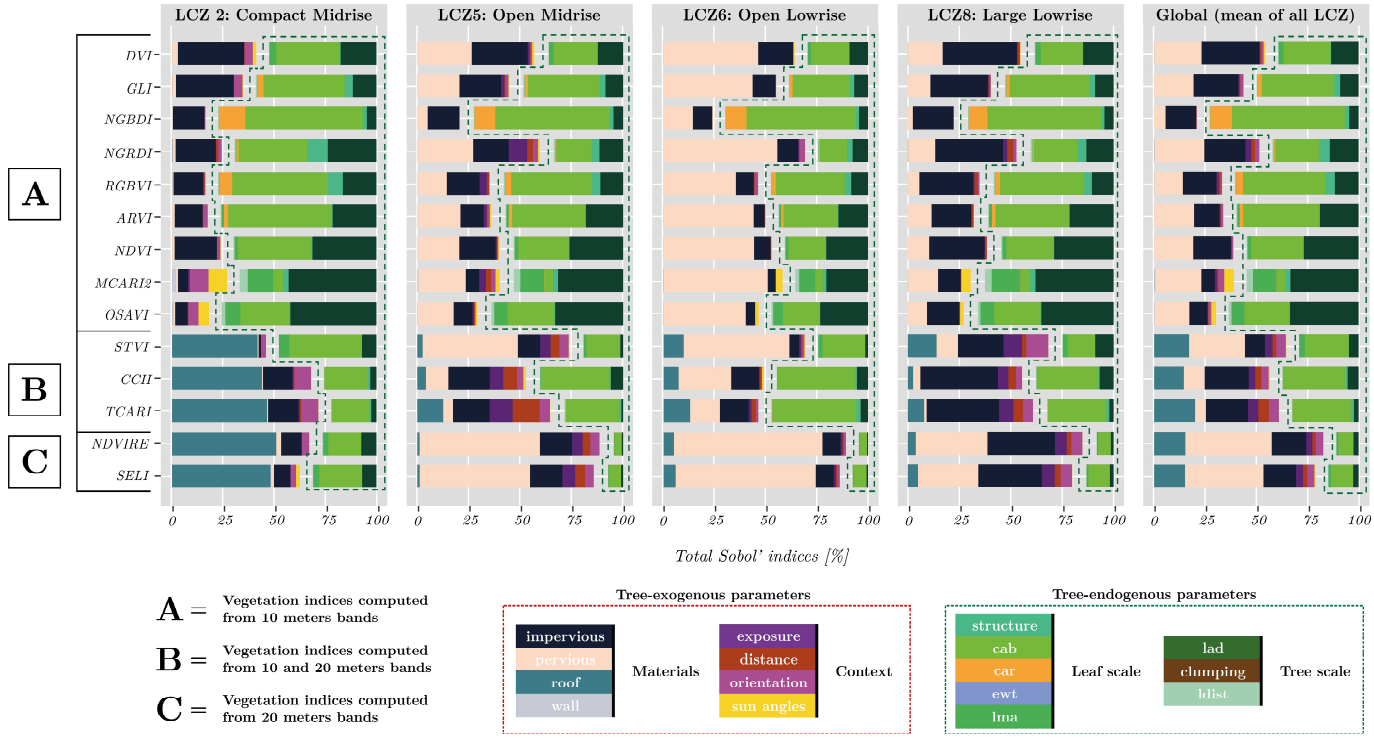

Figure 8. Sobol' indices for SC1 according to the local climate zone (LCZ) and vegetation index, as well as in all LCZs combined.

The VIs calculated at 20 m had the same trend as the spectral bands, with the tree-exogenous parameters having a larger influence at a 20 m resolution than at a 10 m resolution, especially for ground and roof materials (both 55–81%). Likewise, their relative influence varied among the LCZs: in LCZ2, VIs were influenced most by roof materials, whereas in LCZ5, they were influenced most by context parameters such as distance to the nearest building and street orientation. However, TCARI and CII were highly sensitive to one tree-endogenous parameter: Cab. None of the VIs were very sensitive to LAD (mean relative influence of 5%).

At a 10 m resolution, the accuracy of the VIs was assessed by grouping them into three categories—normalized indices with only visible bands, normalized indices with all bands, and complex multispectral infrared indices—with DVI showing the smallest tree-endogenous relative influence (Table 4, Figure 8). The mean relative influence of the tree-endogenous parameters on the four normalized indices with only visible bands was 78% for NGBDI, 64% for RGBVI, 52% for GLI and 45% for NGRDI. While NGBDI was the only one slightly sensitive to Car, all VIs were sensitive to both LAD and Cab, and mainly to the latter. NGBDI had the largest mean relative influence of Cab (60%), regardless of the LCZ, unlike the three other normalized VIs, which had only visible bands that were sensitive to the pervious ground percentage, as seen when comparing the relative influences in LCZ2 and LCZ6 (Table 1). The mean relative influence of tree-endogenous parameters on the two normalized indices for all bands was 63% for ARVI and 61% for NDVI. Specifically, Cab and LAD had a relative influence of 40% and 20%, respectively, on ARVI, and 27% and 27%, respectively, on NDVI. These two VIs were also sensitive to the pervious ground percentage, which caused the relative influence of Cab on ARVI in LCZ2 to LCZ6 to decrease from 55% to 28%, respectively, and its influence on the NDVI to decrease from 40% to 20%, respectively. The mean relative influence of tree-endogenous parameters on the two complex indices with all bands varied the most. While both were the most sensitive to LAD (35% relative influence), their sensitivity to *Cab* and LMA differed, with Cab and LMA having a mean relative influence on MCARI2 of 3.5% and 14%, respectively, and an influence on OSAVI of 9% and 25%, respectively. MCARI2 was the

only VI that was sensitive to LMA. MCARI2 and OSAVI were also sensitive to the pervious ground percentage.

In summary, NGBDI had the highest sensitivity to Cab, ARVI and NDVI had high sensitivity to *Cab* and *LAD*, MCARI2 and OSAVI had the highest sensitivity to LAD (particularly in LCZ6), and TCARI and CCII had little sensitivity to soil material variability, although these last two VIs were generated from 20 m bands.

3.2. Sensitivity Analysis of the Simulated Tree Row Scenario (SC2)

The sensitivity analysis of scenario SC2 was performed for the four window types by considering the central tree of the row as the target tree and the neighboring tree as the neighboring tree. The tree-endogenous parameters were thus assessed according to whether they concerned the target tree or neighboring tree (Trees A and B, Figure 4) (Figure 9).

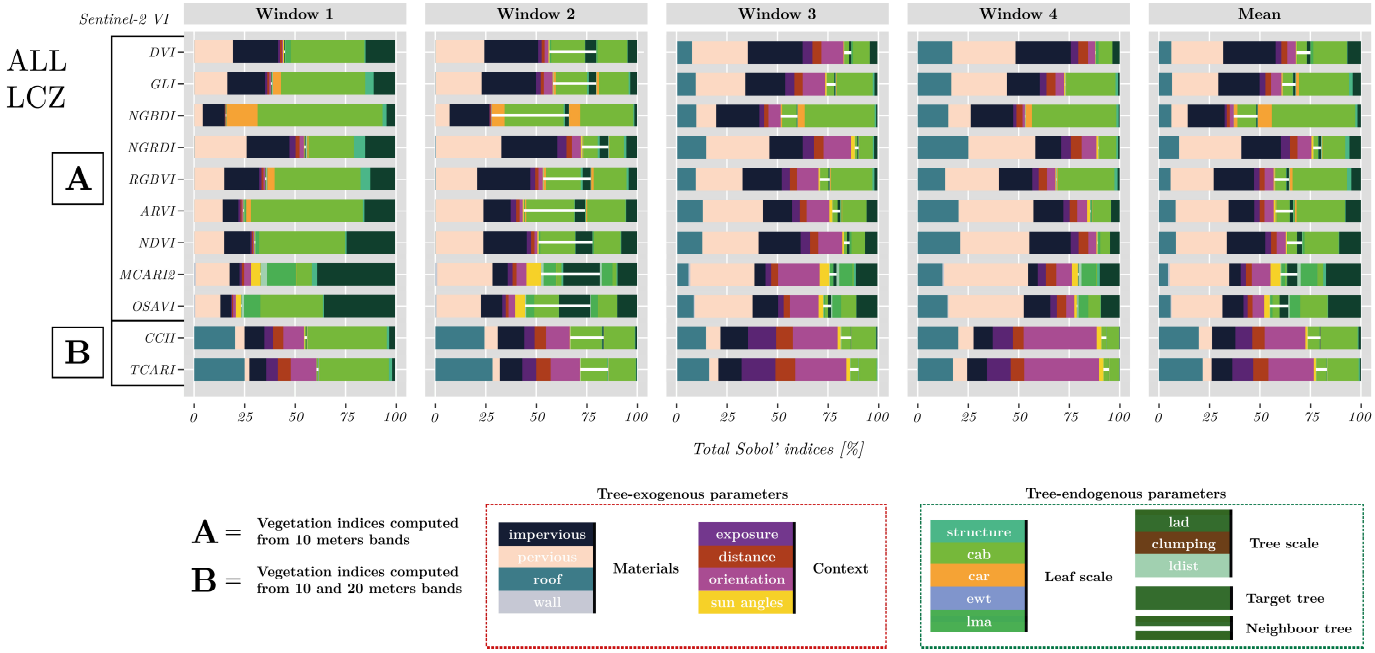

Figure 9. Mean Sobol' indices for scenario SC2 for 11 vegetation indices by local climate zone (LCZ) and window type, as well as for all window types combined (mean).

The sensitivity analysis by window type for SC2 highlighted that the relative influences of the VIs differed among the windows. The relative influences of tree-endogenous parameters for window 1 were slightly larger for SC2 (from 39% for TCARI to 84% for NGBDI) (Figure 9) than for SC1 (from 39% for TCARI to 77% for NGBDI) (Figure 8). The effect of the neighboring tree was assessed by comparing the mean relative influence of all parameters in all LCZs in SC2 (Figure 9) to that of all parameters in all LCZs in SC1 (Figure 8).

Comparing the mean relative influence of tree-endogenous parameters for window 1 (one centred tree) and window 4 (one non-centred tree), which had 78% and 39% canopy cover, respectively, showed a decrease that was proportional to that of canopy cover, ranging from −60 percentage points for ARVI to −31 percentage points for TCARI (Figure 10). Logically, the tree-exogenous material parameters had larger relative influences for window 4 than for window 1. In particular, window 4 in LCZ2 was strongly influenced by roof materials, as a pixel offset perpendicular to the tree row with a short distance to the nearest building was more likely to generate a larger relative influence of roof materials. The relative influence of tree-exogenous parameters for window 4 was strongly influenced by the pervious ground percentage in LCZ6 and LCZ5 and impervious ground percentage in LCZ8. Contextual

parameters also had a notable influence on the VIs for window 4, mainly in LCZ2, LCZ5 and LCZ8, in part due to the large number of buildings and tree shadows (Figure 10).

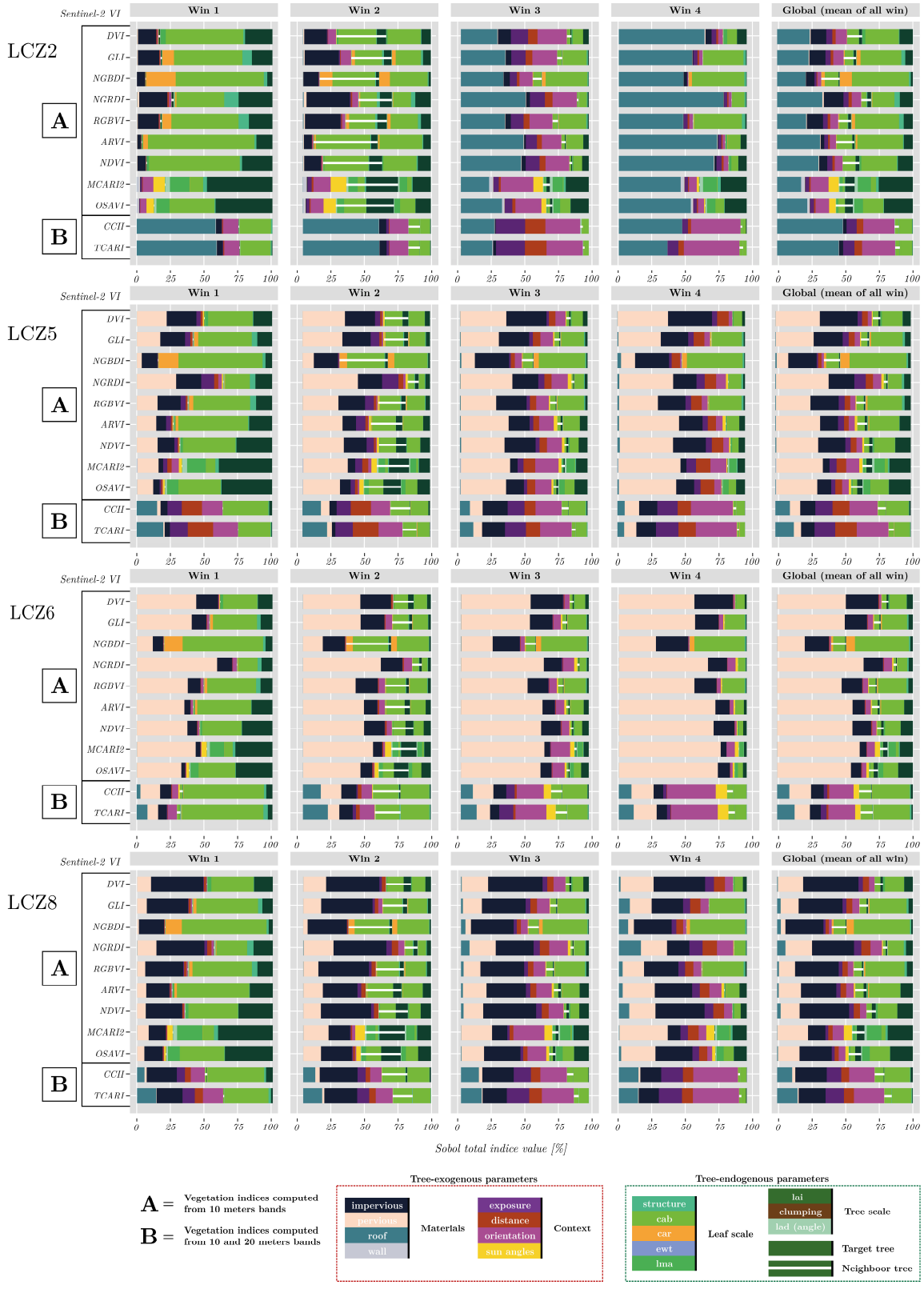

Figure 10. Sobol' indices for scenario SC2 for 11 vegetation indices by local climate zone (LCZ) and window type, as well as for all window types combined (mean).

The effect of the neighboring trees on the mean relative influence of tree-endogenous parameters was observed for window 2, which contained an equal percentage of two trees, and to a lesser extent for window 3, which contained unequal percentages of two trees. For window 2, the relative influence of the target tree was nearly equal to that of the neighboring tree, as both trees had the same canopy cover in the pixel (39% per tree). For example, the relative influence of Cab on NGBDI in LCZ5 was 28% and 30% for the target and neighboring tree, respectively. Although windows 1 and 2 had the same total canopy cover (78%), tree-endogenous parameters had a larger influence for window 1 than for window 2. For most VIs, this difference was larger in LCZ5 and LCZ6 (Figure 10), which had the largest pervious ground percentage. This result highlighted that even if two trees have the same canopy cover in a pixel, the relative influence of their tree-endogenous parameters on VIs can differ, depending on the LCZ type. For window 3, the relative influence of tree-endogenous parameters also included that of the neighboring tree (2–8%), and the orientation was strengthened, especially in LCZ2.

The sensitivity analysis of scenario SC2 revealed that the VI most sensitive to *Cab* and *LAD* depended on the LCZ (Figure 10). For example, in LCZ2, NGBDI, RGBVI and ARVI showed high sensitivity to total Cab (i.e., for both target and neighbouring trees) (52%, 38.5% and 45%, respectively), while MCARI2 and OSAVI were the most sensitive to LAD (32% and 27%, respectively). Similar sensitivity trends were observed for these five VIs in the other LCZs.

However, tree-endogenous parameters could have a relatively small influence, especially for windows 3 and 4 (mixed pixels) in LCZ6. For example, the relative influence of Cab on ARVI for window 4 and in LCZ6 was only 6% due to the influence of the pervious ground percentage (underlying grass vegetation) on most VIs. In contrast, the relative influence of Cab on NGBDI for window 4 and in LCZ6 was 40%, as NGBDI was influenced less by the pervious ground percentage than the other VIs were.

Based on the overall accuracy, six VIs generated from the 10 m resolution bands were considered for further analysis, including NGBDI and RGBVI for Cab, and MCARI2 and OSAVI for LAD. ARVI and NDVI were also considered given their overall accuracy associated with tree-endogenous parameters, and because NDVI is one of the VIs most used and best known for studying vegetation using Sentinel-2 images.

3.3. Comparison of Simulated and Real Data

The 50% and 10% matching methods indicated that the simulated and real spectral bands differed little overall (RMSE = 0.030 and 0.016, respectively). However, the median RMSE for all species combined obtained with the 10% matching method varied from 0.011 for window 4 to 0.034 for window 2 (Figure 11, Appendix B), and also varied for a given window type among species. For example, for window 3, the median RMSE ranged from 0.02 for QR to 0.05 for PL. Moreover, certain species had a wide interquartile range, such as QR for window 1 (0.02) and PL for window 3 (0.05).

The 50% matching method showed slightly more scattered point clouds than those obtained with the 10% matching method for all species, windows and VIs, with a decrease in the overall r values of −0.20 (Figures 11 and A3).

Here, we present a comparison of the simulated and real VIs only for the 10% matching method, considering tree species, Cab and LAD, successively. See Appendix B for the results obtained with the 10% and the 50% matching method (Appendix B: Tables A2–A5).

The correlation between simulated and real VIs for the tree species illustrated that their point clouds varied among the window types (Figure 12). For window 1, ARVI and NDVI were moderately to strongly correlated (r = 0.40–0.85), with a scattered pattern due to DART over-estimates, especially for the NDVI of PL (r = 0.53) compared to that of AC, FR and QR (r = 0.79, 0.99 and 0.85, respectively) (Table A2). RGBVI was even more scattered, with many DART over-estimates. In contrast, NGBDI had a moderate correlation (r = 0.55–0.85) but a scattered pattern due to DART under-estimates.

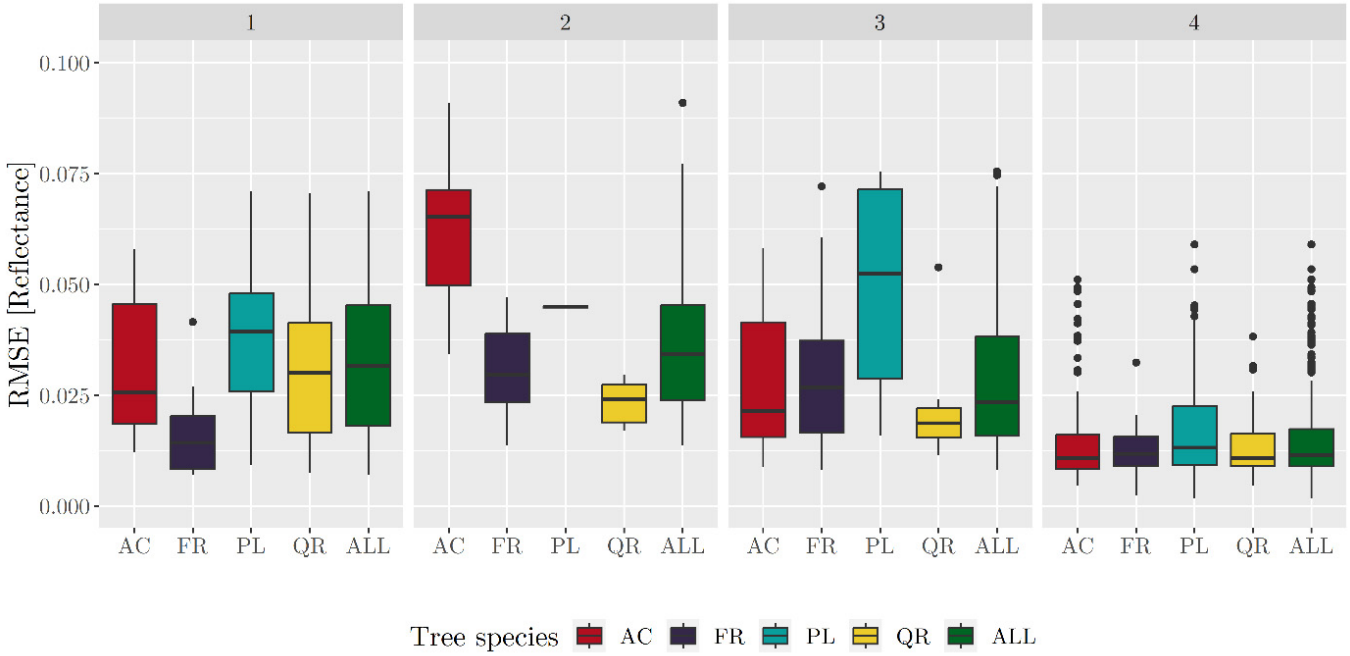

Figure 11. Distribution of root mean square error (RMSE) between simulated and real Sentinel-2 spectral bands per species (i.e., Acer platanoïdes (AC), Fraxinus excelsior (FR), Platanus acerifolia (PL) and Quercus rubra (QR)) and window type (i.e., 1–4), calculated using the 10% matching method. Error bars represent 1.5 times the interquartile range.

For window 2, the VI values were less correlated and were widely scattered for all VIs, with r ranging from 0.05 for RGBVI to 0.28 for NDVI (Figure 12). DART greatly underestimated NGBDI and greatly over-estimated RGBVI, MCARI2 and OSAVI. However, some species had a stronger correlation, such as AC, with 0.52 and 0.57 for ARVI and RGBVI, respectively, and FR, with 0.61 and 0.58 for OSAVI and MCARI2, respectively. Window 3 also showed substantial scattering, but with slightly stronger correlations for all species than those for window 2. Window 4 had the strongest correlations and smallest RSME between the simulated and real VIs (i.e., $r > 0.96$ and RMSE < 0.04). The VI values were narrowly distributed along the 1:1 line, particularly for NDVI and ARVI (r = 0.25–0.90).

The correlation between simulated and real VIs as a function of Cab and LAI varied (Figures 13 and 14. For windows 1 and 4, the pixels corresponding to trees with a high Cab (>36 $\mu g/cm^2$) and LAD (>0.8) lay more closely along the 1:1 line, while deviations from it corresponded to pixels with a lower Cab (<28 $\mu g/cm^2$) and LAD (>0.8). For Cab, this was particularly true for NGBDI, ARVI and NDVI, unlike for RGBVI, whose points with a high Cab were more scattered. In general, the higher the chlorophyll content of the tree in the pixel, the more accurate were the DART-simulated VI values. For LAD, this was particularly true for MCARI and OSAVI.

The results obtained using the five Sentinel-2 dates from 6 June (DOY = 156) to 5 September (DOY = 248) 2021 did not show that solar illumination had an influence (i.e., sun angles, shadows). The metrics calculated for all windows on each DOY were similar to those calculated for all windows and all DOYs and that for all VIs (Tables A4 and A5), except for the image of 5 September, which had negative correlations for window 2.

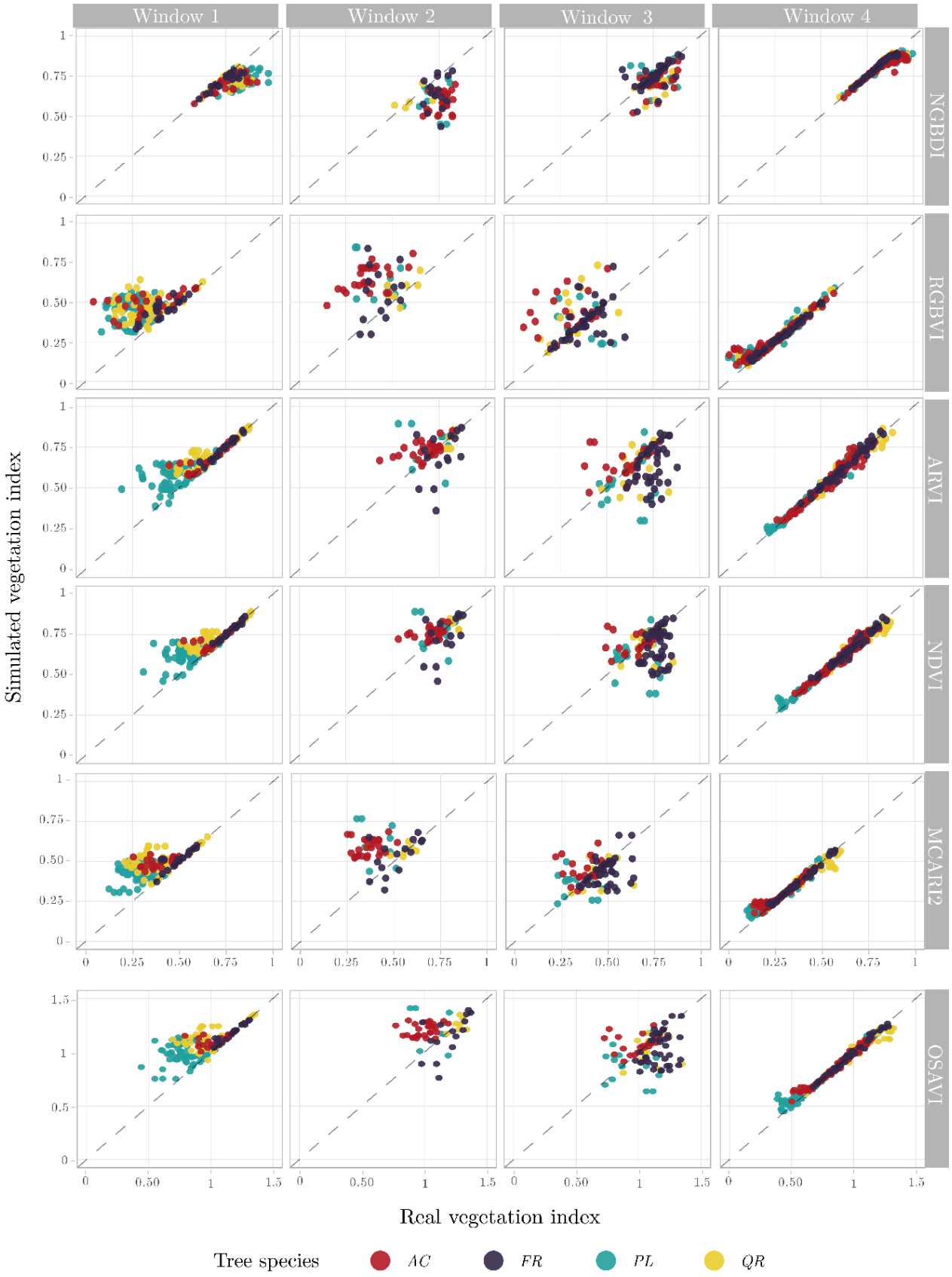

Figure 12. Scatter plots of real and simulated Sentinel-2 vegetation indices by type of extraction window according to the 10% matching method. AC: Acer platanoïdes, FR: Fraxinus excelsior, PL: Platanus acerifolia, QR: Quercus rubra.

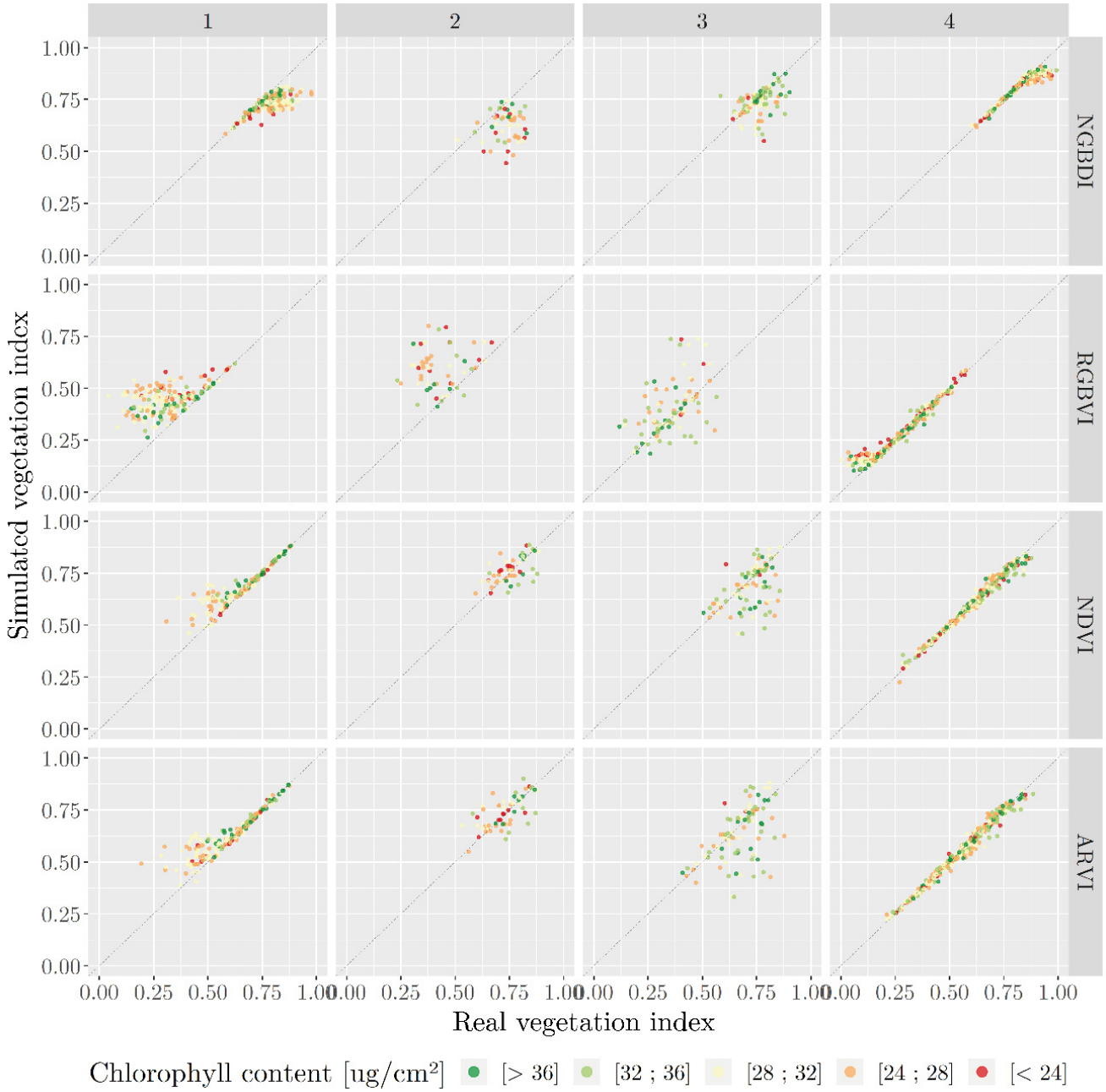

Figure 13. Scatter plots of real and simulated Sentinel-2 vegetation indices by type of extraction window according to the 10% matching method. For each point, the measured chlorophyll content of the tree(s) corresponding to the pixel is shown.

In summary, considering all species and windows (environmental conditions), the strongest correlations between simulated and real data were found for window 4 (one tree with low canopy cover) and window 1 (one centered tree). For window 4, the correlations were strong for all four species ($r > 0.98$). The strongest correlations were observed for window 1 for ARVI, for FR ($r = 0.99$ and RMSE = 0.01), followed by AC ($r = 0.86$ and RMSE = 0.05), QR ($r = 0.87$ and RMSE = 0.07) and PL ($r = 0.63$ and RMSE = 0.12).

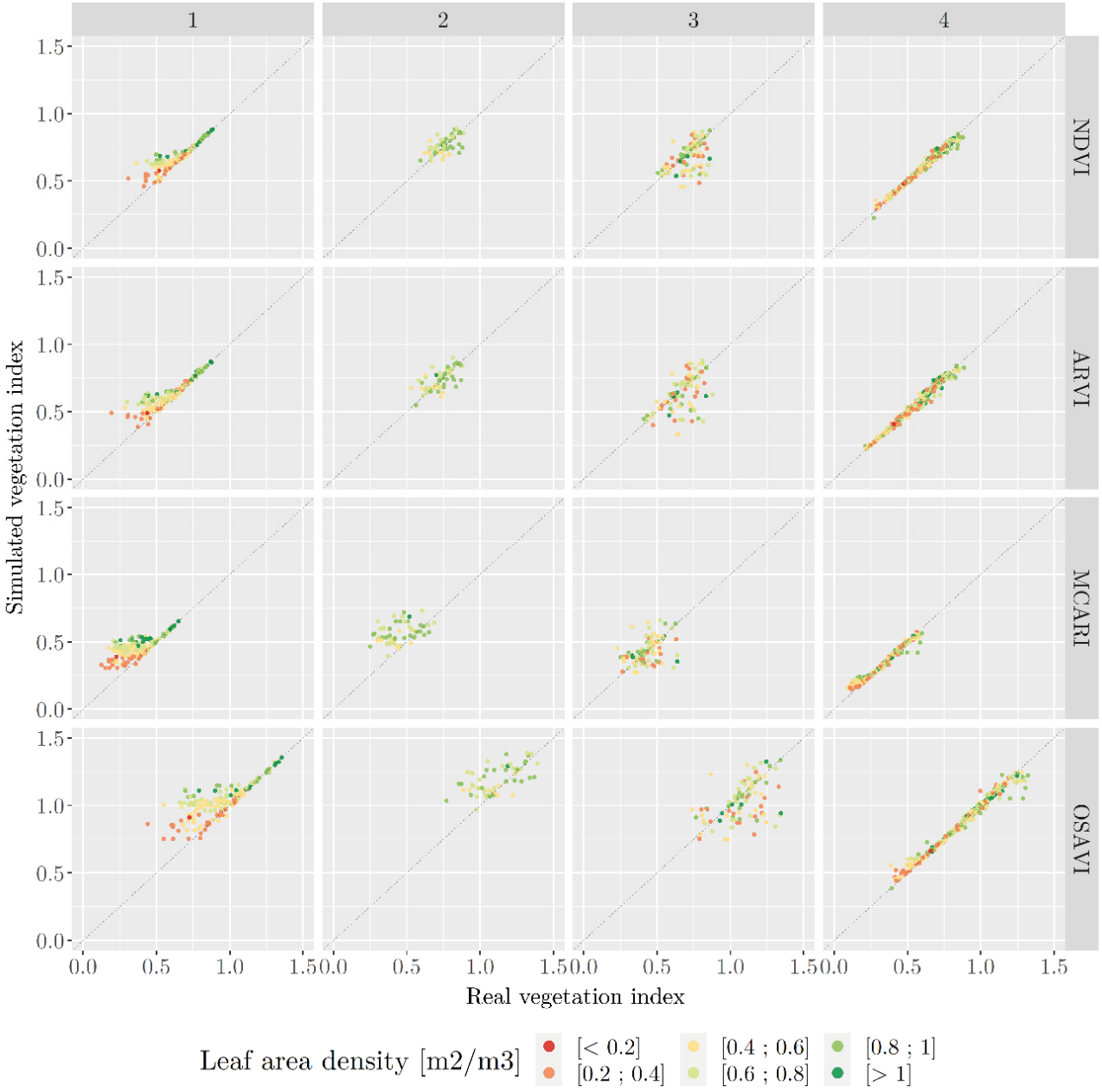

Figure 14. Scatter plots of real and simulated Sentinel-2 vegetation indices by type of extraction window according to the 10% matching method. For each point, the measured leaf area density of the tree(s) corresponding to the pixel is shown.

4. Discussion

4.1. Modelling Assumptions and Choice of LCZs

The experimental design for simulating Sentinel-2 data using DART and LCZs was based on several assumptions and used simplified reference data on urban trees, which led to certain limitations that may explain the differences observed between the simulated and real data. Specifically, these differences could be explained by the tree-endogenous and tree-exogenous parameters chosen, as well as the use of the LCZ taxonomy.

4.1.1. Tree-Endogenous Parameters

The geometric characteristics of trees were determined based on a reference database at a height of 15 m and a diameter of 10 m. These dimensions sometimes differed from those of the real trees studied, depending on the species. The median height of the AC,

QR and FR of real trees ranged from 13.5 to 14.0 m, while that of PL was 6.5 m; the height was up to 22 m for certain PL trees. Similarly, the median crown diameter of real trees also varied, from 10 m for QR and FR to 11.5–12.0 m for PL and AC. Moreover, the crown shape of simulated trees was a perfect circle, whereas that on the Sentinel-2 images was more irregular. The median circularity ($\frac{4\pi Crown_{area}}{Crown_{perimeter}{}^2}$) of simulated trees was 1 (which corresponds to a circle), whereas that of real trees was 0.55 for PL and close to 0.70 for AC, FR and QR. In the simulations, the crown volume was represented by an ellipsoid. Among the four tree species studied, the crowns of QR and AC corresponded to an ellipsoid, while those of PL and FR were more V-shaped. These differences in geometric characteristics observed between the simulated and real trees influenced tree radiation interception, and thus the first-order influence of top-of-canopy reflection and the second-order influence of the reflection of transmission through the tree crown (i.e., light-path lengths depend on the crown shape) [90] and background reflection. Tree structure also determined the percentage of woody elements in the crown, as branch shape, length and density can strongly influence reflectance [67,91,92], especially during periods of low LAI. In addition, the structure of urban trees also depended strongly on the type of pruning and the branching habit.

For most VIs, we observed that the simulated data were accurate for FR, whose geometry was more similar to that of the simulated reference tree, and that they were less accurate for PL, whose geometry differed greatly from that of the simulated reference tree.

4.1.2. Tree-Exogenous Parameters

The urban environment contains a wide variety of materials. The spectral library used in the experimental design (i.e., roof, wall, mineral soil and plant soil materials), although non-exhaustive, varied greatly. However, two parameters were not considered. The first was the diversity and height of underlying vegetation: while grass areas usually consist of a mixture of green and dry grass that can vary in composition and structure, only two contrasting spectra were used in the simulations; this was instead of a gradient of spectral mixes with specific phenological dynamics. The second parameter was the diversity of mineral materials: only one mineral ground type was selected for each simulation, whereas that in urban spaces can be heterogeneous, even at a 10 m resolution. In addition, the results showed that walls had a small influence on reflectance, as the building models were simple and did not include windows, which have a specular reflection, unlike the Lambertian materials used in the simulations. In certain configurations, windows can have a non-negligible effect on the radiation balance at the street scale [93]. We also assumed that the atmosphere was unpolluted, with a low optical thickness, whereas in reality it can be polluted near trees at the scale of an urban canyon, which can strongly influence short-wavelength spectral bands and influence the calculation of certain VIs based on B02 (blue wavelengths).

The images were simulated with fixed gas and aerosol properties (optical, chemical, thermal and geometric). However, at the city scale and depending on climate, these conditions can vary greatly in time and space, influencing the reflectance values of Sentinel-2 images [94]. In this study, their influence on Sentinel-2 images was not quantified, assuming that the atmospheric correction was performed optimally. Future research could include the variations in aerosol abundance and atmospheric water vapor content, for instance, to quantify the impact of pollution and atmospheric moisture, respectively, and to expand the results to cities located in tropical and desertic areas or those with strong industrial activity.

4.1.3. The LCZ Approach

LCZs were used as a framework to represent four contrasting 3D urban scenes. The geometric characteristics of buildings (i.e., volume, height and layout) determine how shadows are projected. The percentages of mineral ground and grass, which varied among the LCZs, also strongly influenced the reflectance and VIs. LCZ2 is characterized by narrow streets with high buildings, so the most influential tree-exogenous parameters are contextual parameters (i.e., orientation, exposure, distance and solar angles) and roof

materials, which had a large influence on the reflectance and VI values. While LCZ5 is characterized by high buildings with wider streets, the influence of shading is still important, but depends more on the position of trees in relation to buildings. In contrast to these two LCZs, in LCZ6 and LCZ8, the influence of buildings is less important than that of ground vegetation and ground materials. While LCZ maps are now widely available, they can be used for Sentinel-2 data processing, taking into account the specificity of each LCZ. For example, shading or vegetation understory effects could be reduced in LCZs 2 and 5, and in LCZ6, respectively, which is important for time series consistency for urban tree monitoring.

We generated 100 × 100 m 3D urban scenes at a 1 m resolution, as the automatic LCZ calculation method used most provides data at a 100 m resolution [95]. Hence, although LCZ is usually considered as a local approach [59], it remains coarser than Sentinel-2's spatial resolution. The LCZ classification was used to provide a framework for constructing pseudo-realistic urban scenes. However, the approach chosen for modeling the urban environment is discrete, whereas the urban environment is continuous. At the scale of a 100 × 100 m scene, buildings can be highly variable in size and materials, limiting the use of LCZs at fine scales. Using a digital twin that includes buildings, street features, topography and materials would enable researchers to assess the physical, structural and optical properties of urban scenes and more accurately determine the mixture within a Sentinel-2 pixel. Thus, the building layout in the LCZ directly influences the mixture in a pixel. This effect was obvious for the 20 m bands in LCZ2, in which roof materials equaled nearly 80% of the total influence, because the street was narrow and roofs covered most of the pixel.

In addition, the LCZ approach does not allow the layout or location of trees to be specified within 3D scenes. Although we assessed two types of tree layout in the two scenarios and four contextual variable parameters, these 3D scenes represented only some of the tree layouts actually encountered in a city, such as double tree rows and non-linear tree rows.

4.2. Sensitivity Analysis Based on Simulated Data

4.2.1. VI Performances to Characterize Functional Traits of Trees

The sensitivity analysis showed similar results for isolated trees (SC1) and tree rows (window 1 for SC2). In other words, neighboring trees have a negligible indirect effect when the pixel is centered on the target tree. It also demonstrated that Cab and LAD were the tree-endogenous parameters that influenced Sentinel-2 spectral bands and VIs the most. To a lesser extent, Car and LMA, respectively, influenced B02 reflectance and its derived index NGBDI, and B08 reflectance and its derived indices (especially MCARI2). The results of the sensitivity analysis for the VIS and NIR bands at a 10 m spatial resolution are consistent with those obtained in a study focusing on a homogeneous canopy simulated with PROSAIL [96]. The latter showed that Car was dependent on B02, Cab almost exclusively on VIS bands, and LAI and LMA on NIR bands. However, our results diverged with respect to the influence of vegetation traits on bands at a 20 m spatial resolution (RE and SWIR), due to the sub-pixel heterogeneity in urban areas. For example, our results showed that EWT did not affect SWIR bands, which are predominantly influenced by ground and building roof materials.

NGBDI and ARVI were among the most accurate indices and influenced the most by Cab. However, the high accuracy of NGBDI raises concerns regarding the use of band B02 in an urban environment due to its sensitivity to aerosols [72]: a small change in reflectance can change the index greatly due to the status of the atmosphere compared to Cab. This could explain the differences observed between the simulated and real NGBDI values. The results also showed a particular pattern of sensitivity for MCARI2, with a strong influence of *LAD* and negligible influence of *Cab*. This pattern is consistent with the theoretical assumptions used to calculate MCARI2, which was included to maintain maximum sensitivity to LAI while decreasing the influence of variability in chlorophyll [97].

The correlations between the DART-simulated and real VI values were good. However, the comparison raises several questions about the field dataset used. Cab ranged from 11 to 45, but a saturation effect may have occurred when it exceeded 45, which may have weakened the correlation. Moreover, DART simulates LAD, but the corresponding parameter measured in the field was actually the plant area density (PAD) (i.e., including both leaves and branches). Consequently, we can deduce that over-estimated real values (PAD field measurements) were used when compared with DART LAD values.

One of the most important results revealed by the sensitivity analysis was the large influence of the grass ground percentage on the reflectance and VIs (except for NGBDI), as illustrated in LCZ6, which had the largest grass ground percentage (50%). This sensitivity could limit tree studies. For example, grass ground had a larger influence for window 3 than for window 4, which showed that the reflectance and VIs were influenced more by the dynamics of the underlying grass than by those of the tree. In this case, data on the grass at a high spatial resolution may help assess the sensed signal, because trees and grass can have a similar spectral shape but different temporal dynamics [98].

4.2.2. Influence of the Radiative Transfer Model Chosen

Sensitivity analysis is often used with radiative transfer models. The sensitivity of Sentinel-2 images to vegetation traits has been studied using PROSAIL, which is a 2D/2.5D radiative transfer model, for homogenous canopies [42,96,99,100]; meanwhile, INFORM or DART have been used for more complex and rougher canopies [52,101]. As most studies have focused on tree-endogenous parameters, few have considered vegetation-exogenous parameters such as the solar angle or soil moisture. For tree-endogenous parameters, the sensitivity patterns of spectral bands in the present study were similar to those in the literature: B02 was the only one that was sensitive to Car, B03 was the most sensitive to Cab, B04 was the most sensitive to Cab and LAI, and B08 was the most sensitive to LMA. Cab and LAD also influenced VIs such as NDVI.

One major advantage of this study was that it considered both endogenous and exogenous parameters using DART. In a previous study, a sensitivity analysis that compared DART and PROSAIL showed that DART outputs were more sensitive to one vegetation-exogenous parameter—the solar angle—than PROSAIL outputs [101]. This demonstrated the importance of representing 3D scenes to consider the effects of light interception and shadows, which are strong in heterogeneous urban areas. The present study assessed eight tree-exogenous parameters in the sensitivity analysis; its results demonstrated that tree-exogenous parameters usually had more influence on spectral bands and VIs than tree-endogenous parameters did.

Including tree-exogenous parameters in the sensitivity analysis, combined with the LCZ and extraction window approach, highlighted the importance of two key elements that influence spectral bands and VIs: a tree's planting conditions and a pixel's composition (i.e., percentages of vegetation and various materials). Thus, ancillary data should be used along with Sentinel-2 images to capture the heterogeneity in urban areas. For example, one can use the tree crown extent to calculate the canopy cover and the number of trees per pixel, the extent of underlying vegetation (to estimate the percentage of grass per pixel) and the types of ground materials; this can also be used to create a digital surface model that quantifies the canopy height to calculate the percentage of shadow cast per pixel on a given date.

4.3. The Extraction-Window Method for Capturing Pixel Heterogeneity in Urban Areas

The results highlighted the difficulty of studying tree functional traits when the objects of interest (i.e., urban trees) have the same area as the pixel. Specifically, the creation of a relationship of scale among field measurements at the leaf scale, field measurements extrapolated to the canopy scale and pixel values at a coarser scale is challenging [102]. The window approach merges the two most common approaches (object-based or pixel-based approach) used to extract pixel values [103]. While the object-based method summarizes

data and can reduce information and/or induce noise, the pixel-based method assumes that the pixel is pure and that the object of interest covers it entirely, which is not necessarily true. For urban trees, values should not be aggregated, as the scenes are heterogeneous, and given the small size of the objects of interest and the potential offsets during orthorectification, doing so is unlikely to yield pure pixels. The window method provides an initial way to address these difficulties. It preserves image values without interpolation or aggregation, but still considers a pixel's heterogeneity and associated uncertainty.

We used the extraction window method, which assigns window types to pixels based on the spatial coverage of tree crowns. We determined the uncertainty caused by the extraction conditions and the influence of the parameters on monitoring and estimation as a function of window type. The results highlighted the good accuracy of the DART-simulated Sentinel-2 values, especially for windows 1 and 4, which contained only a single tree. The accuracy was lower for windows 2 and 3, perhaps because the characteristics of two trees did not have additive effects; for example, Cab and LAD showed a non-additive effect at the scale of two tree crowns.

While the extraction window method allowed us to consider four different pixel types according to their percentage of canopy cover and number of trees, ancillary data could be used to mitigate the issue of mixed pixels in a continuous and more comprehensive way. Specifically, ancillary data can be used to characterize pixels both quantitatively (e.g., proportion of cover types or materials) and qualitatively (type of cover or material). For example, the canopy cover per pixel can be extracted from vector data (as in this study) or from canopy height models, which are now increasingly available at very high spatial resolutions and on a large scale [104,105]. The proportion of shadows per pixel, resulting from the exposure of parameters, the distance between trees and buildings, and street orientation, can be determined from the combined use of a digital surface model and geospatial modelling tools such as the potential incoming solar radiation tool available in SAGA [106]). These pixel characteristics can be used to filter a set of pixels corresponding to specific conditions (e.g., pixels with high canopy cover and without shadows), or can be integrated as input features in vegetation trait estimation models.

5. Conclusions

This study, which focused on assessing the suitability of Sentinel-2 images for characterizing two functional traits (Cab and LAD) of urban trees, highlighted the strong influence of tree-exogenous and tree-endogenous parameters on Sentinel-2 spectral bands at a 20 m and 10 m resolution, respectively, whether the trees were considered individually or in rows. It also identified the VIs that were most sensitive to Cab and LAD among environments or pixel configurations. The comparison of DART-simulated and real Sentinel-2 data, which also included field measurements and ancillary data, showed good accuracy both for spectral bands and certain VIs, which highlighted the value of ancillary data to better capture specific urban characteristics, such as canopy cover, the percentage of underlying vegetation and ground materials. This study identifies three main perspectives. The first perspective focuses on the precision of physical modelling for the sensitivity analysis. Several aspects remain to be investigated, such as the more realistic modelling of trees and a more comprehensive consideration of atmospheric and aerosol variability. The second perspective involves the development of a model for estimating the Cab and LAI of urban trees based on the inversion of the DART model and Sentinel-2 imagery, considering, as input data, the VIs most influenced by LAI and Cab (highlighted in this study) and the tree-exogenous parameters (underlying vegetation, shading, materials) derived from auxiliary data. The third perspective is concerned with the temporal analysis of VIs, Cab and LAI parameters, which could reveal relationships between tree species and the factors associated with urbanization, such as urban heat islands or soil imperviousness. Addressing these issues could lead to a deeper understanding of the interactions between endogenous tree parameters, the urban environment and satellite imagery, and thus to an improvement in urban tree monitoring using remote sensing data.

Author Contributions: T.L.S.: Conceptualization, visualization, methodology, investigation, writing—original draft; J.N.: Conceptualization, methodology, investigation, project administration, funding acquisition, supervision; S.L.: Methodology; J.-P.G.-E.: Methodology; L.H.-M.: Supervision, writing—review and editing; K.A.: Conceptualization, methodology, investigation, supervision, writing—review and editing. All authors have read and agreed to the published version of the manuscript.

Funding: This study was supported by Rennes Métropole and the Association Nationale de la Recherche et de la Technologie (ASTRESS project and grant No. 2021/0301).

Data Availability Statement: Field survey data for Cab and LAD measurement are available at https://zenodo.org/records/12751353.

Acknowledgments: This article is a revised and expanded version of a paper entitled "Sensitivity analysis of Sentinel-2 data for urban tree characterization using DART model" [107], which was presented at [SPIE Remote Sensing, Amsterdam, The Netherlands, 3 September 2023]. The authors acknowledge Julien Pellen for the preprocessing of the Sentinel-2 images.

Conflicts of Interest: The authors declare no conflicts of interest.

Appendix A. Detailed Description of DART Input Parameters

Appendix A.1. Tree-Exogenous Parameters

Appendix A.1.1. Sensor Settings, Direction Input Parameter and Atmosphere

The illumination of the scene is important, as it determines the distance of the shadow cast by the buildings (and the energy balance of the scene). These conditions change throughout the year, characterized by a change in the solar incidence angles (zenith and azimuth). To reproduce this change, the date can be set in DART (which will determine the solar angles for a given latitude and longitude) and then changed. We considered dates from 15 March to 15 November, which coincides with the vegetative period of the trees. Concerning parameters for the atmosphere, urban areas have a specific atmosphere because the concentration of housing and industry produces large amounts of emissions that influence the composition of the atmosphere and aerosols. Images acquired in urban areas are therefore influenced more by absorption and scattering, mainly in the visible and near-infrared wavelengths. The DART model can use the *USSTD76* atmospheric model [108] to reproduce the atmospheric influence on the signal. The optical properties of aerosols can also be set; this study used an urban aerosol with a constant multiplier of 1 for the optical depth of aerosols. The temperature of the elements in the scene has been set at 300°K.

Appendix A.1.2. Spectral Library

One characteristic of the urban environment is the variety of materials, most of which are human-made or mineral, such as rough stone (e.g., sandstone, limestone), granite, asphalt, cement, concrete, brick, shingle, slate, red tile, and glass, or even metals, such as steel and zinc. Each material has specific spectral signatures due to its intrinsic physical and chemical composition that will influence the land surface radiation balance in the scene, as well as the reflectance of the pixel analyzed. Due to the geometric configuration of the four LCZs selected and the simplified 3D representations of the buildings, and to reproduce plausible contexts that represent a broad range of materials, four classes were considered: roofs, walls, impermeable ground and permeable ground. Each of these classes was assigned potential reflectance spectra from a DART spectral library with different levels of detail. A total of 18 spectra were retained (Figure A1). The four types of surfaces were modelled as Lambertian surfaces.

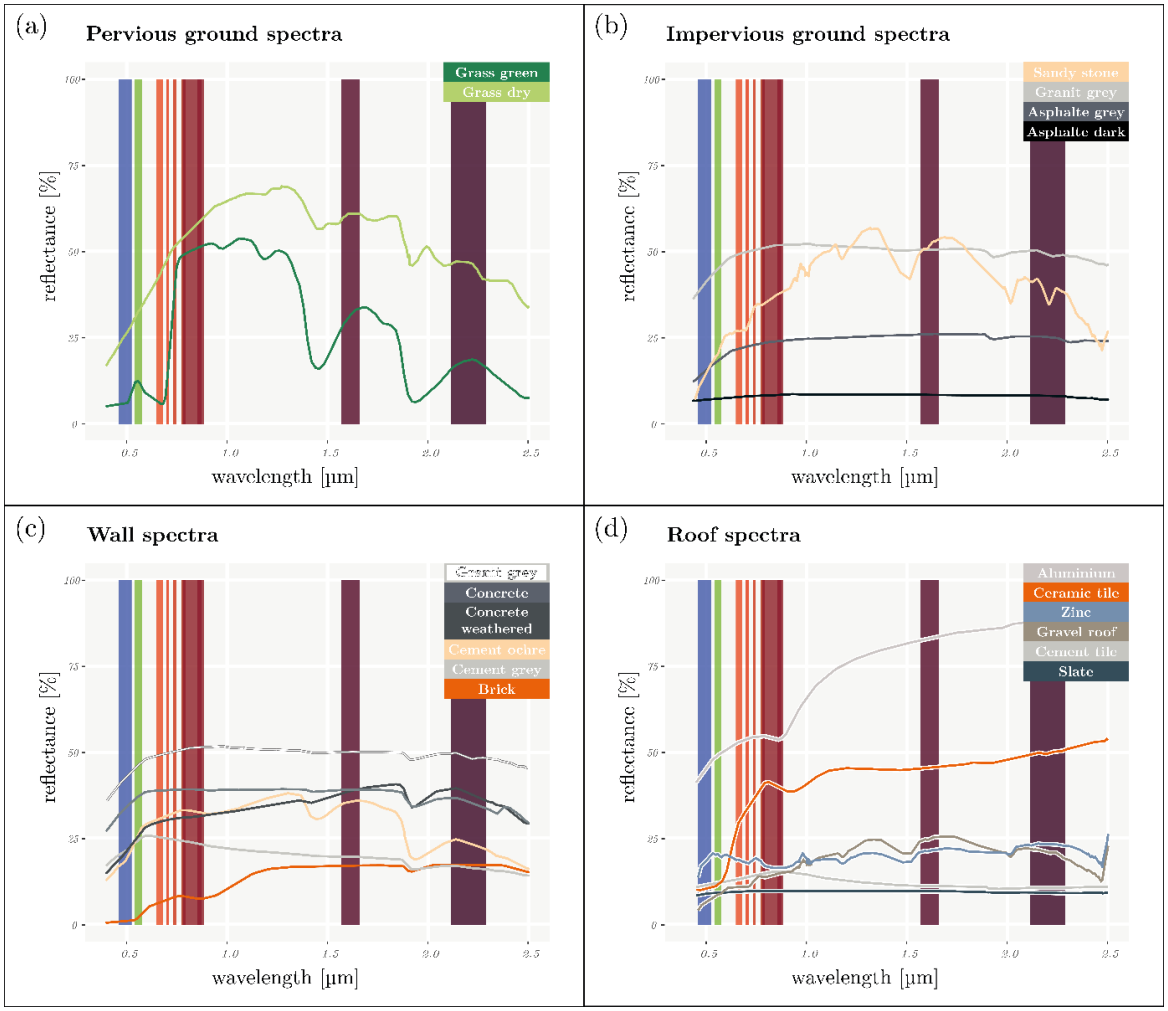

Figure A1. Spectral library showing the four spectral categories for (**a**) pervious ground (n = 2), (**b**) impervious ground (n = 4), (**c**) walls (n = 6) and (**d**) roofs (n = 6). Each spectrum is shown with its reflectance value [%] as a function of wavelength [µm]. The vertical bands correspond to the central wavelength and width of Sentinel-2 spectral bands.

Appendix A.1.3. Earth Scene and Tree Planting Context

The scene was set in Rennes, France, to match the real Sentinel-2 data. The scene dimensions were set to 100 × 100 m based on the scale of LCZs, and to ensure that electromagnetic interactions in the tree's environment could actually occur. The conditions under which a tree is planted are a key factor in its development. It is important to distinguish two elements: the absolute planting conditions, which include the type of ground (e.g., soil, grass, human-made materials) at the base of the tree, and the environmental conditions (e.g., presence of buildings, street). The former can be classified as restricted (a ca. 1 m^2 square of bare soil or grass surrounded by impermeable materials), linear (trees planted on a strip of bare soil or grass surrounded by impermeable materials) or open (trees located on extended grass or in a park) [109]. In the simulations, these conditions were reflected by the ratio of permeable to impermeable ground defined with the LCZs (Table 1). The latter can be described using three parameters: the distance from the tree to the nearest building, the street orientation and the exposure (planted on the sunny or shady side of the street). These three parameters are likely to strongly influence how shade will impact the tree.

Appendix A.2. Tree-Endogenous Parameters

Appendix A.2.1. Tree Structural Parameters

Tree structural parameters were determined by analyzing the tree row database of the Lyon metropolitan area, which is one of the most complete databases for France in OpenData (https://data.grandlyon.com/jeux-de-donnees/arbres-alignement-metropole-lyon/info, accessed on 1 September 2024). The database contains 50,000 records with the following geometric variables: crown height, crown diameter, total height and trunk diameter. To build a reference profile, the database was limited to the five most common genera, namely *Tilia*, *Acer*, *Platanus*, *Fraxinus*, and *Quercus*, which agrees with urban tree databases for other European cities, and to crown diameters of 8–12 m. With these limits, mean values were calculated for tree structural parameters (Table A1). The tree was further modelled with an ellipsoid crown and a cylindrical trunk without branches.

Table A1. Structural parameters of the tree modelled in DART.

Parameter	Value [m]
Tree height	15
Trunk height under the crown	4
Trunk height in the crown	6
Trunk diameter	0.4
Crown diameter	10

Three parameters were variable: leaf area density (LAD), the percentage of crown holes and the leaf angle distribution. The leaf area index (LAI) was calculated as the total leaf area of a canopy per unit area of ground, which is suitable for a tree canopy with a homogeneous height such as that of dense forests. For a single tree, LAI can be defined using the LAD, which equals the total leaf area per unit volume of canopy (i.e., the tree crown) in m^2/m^3. Next, a clumping factor indicates the degree of spatial aggregation of leaves in the canopy. DART can calculate the percentage of crown volume occupied by leaves. If 100% of the crown volume is occupied, the LAD is homogeneous at the crown scale and the clumping factor equals 0, but if only 50% of the crown volume is occupied, the LAD is not homogeneous at the crown scale, and leaves are artificially aggregated for a given initial LAD. We used a crown hole percentage of 0–50% as a proxy to simulate the clumping factor. Finally, the leaf angle distribution refers to the statistical distribution of the angular orientation of leaves at the scale of a tree (e.g., planophilic, plagiophilic, extremophilic, uniform). Several methods exist to estimate it, including several predefined mathematical functions. From the database available in [110], which provides leaf inclination angles for temperate and boreal broadleaf woody species, the two most common distributions (i.e., planophile and plagiophile) for deciduous tree species were extracted.

Appendix A.2.2. Leaf Parameters

The DART model is coupled with the PROSPECT model. In this study, the PROSPECT-D version was used [65], as it can simulate the reflectance and transmittance spectra of a leaf in the spectral range of 0.4–2.5 µm (Figure A2). To simulate these spectra, the model uses seven parameters: the structure coefficient (N), chlorophyll content (Cab), carotenoid content (Car), anthocyanin content, brown pigments, equivalent water thickness (EWT) and dry matter (LMA). The simulated spectrum is then assigned to the optical properties of the tree leaves in DART.

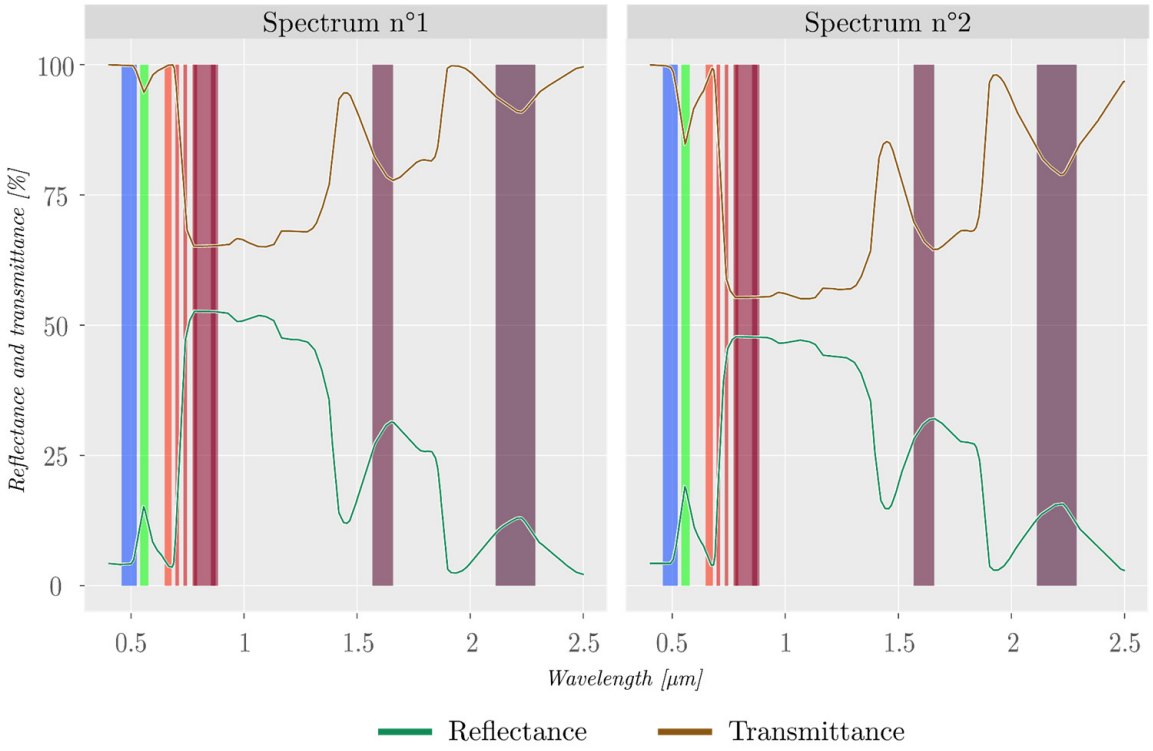

Figure A2. Example of two leaf spectra simulated by the PROSPECT model. Spectrum 1: N = 2.3, Cab = 60, Car = 25, EWT= 0.024 and LMA= 0.018. Spectrum 2: N = 1.7, Cab = 32.5, Car = 13.75, EWT= 0.014 and LMA= 0.008. Spectra 1 and 2 correspond to the maximum and median values used in the virtual experimental design, respectively. The vertical bands correspond to the central wavelength and width of Sentinel-2 spectral bands.

Appendix B. Ancillary Tables and Figures Comparing Simulated and Real Data

Table A2. Pearson correlation coefficient (r) and root mean square error (RMSE) by vegetation index and extraction window (as well as all windows) for each tree species and all species for the 10% matching method.

VI	SP	Window 1		Window 2		Window 3		Window 4		All Windows	
		RMSE	r	RMSE	r	RMSE	r	RMSE	r	RMSE	r
NDVI	AC	0.05	0.79	0.07	0.44	0.10	0.36	0.02	0.99	0.05	0.9
	FR	0.01	0.99	0.12	0.51	0.14	0.27	0.02	0.99	0.1	0.62
	PL	0.11	0.53	0.14	−0.22	0.17	−0.07	0.01	1	0.08	0.81
	QR	0.06	0.85	0.04	−0.07	0.09	0.25	0.02	0.98	0.05	0.86
	ALL	0.08	0.82	0.10	0.28	0.13	0.17	0.02	0.99	0.07	0.84
ARVI	AC	0.05	0.86	0.09	0.52	0.13	0.36	0.02	0.98	0.06	0.89
	FR	0.01	0.99	0.15	0.38	0.16	0.37	0.02	0.98	0.11	0.63
	PL	0.12	0.63	0.18	−0.20	0.18	0.15	0.02	0.99	0.09	0.81
	QR	0.07	0.87	0.04	0.82	0.12	0.34	0.02	0.98	0.06	0.86
	ALL	0.09	0.84	0.12	0.23	0.15	0.27	0.02	0.99	0.08	0.84
NGBDI	AC	0.08	0.69	0.19	0.26	0.10	0.54	0.03	0.94	0.08	0.71
	FR	0.04	0.92	0.14	0.2	0.06	0.57	0.01	0.99	0.06	0.70
	PL	0.10	0.42	0.17	0.01	0.10	−0.12	0.03	0.95	0.08	0.67
	QR	0.07	0.55	0.06	0.68	0.08	0.57	0.02	0.97	0.05	0.8
	ALL	0.09	0.57	0.16	0.11	0.08	0.4	0.02	0.96	0.072	0.7

Table A2. *Cont.*

VI	SP	Window 1		Window 2		Window 3		Window 4		All Windows	
		RMSE	r	RMSE	r	RMSE	r	RMSE	r	RMSE	r
RGBVI	AC	0.2	0.55	0.29	0.57	0.2	0.26	0.04	0.95	0.14	0.71
	FR	0.06	0.85	0.2	0.21	0.1	0.5	0.01	1	0.1	0.73
	PL	0.22	0.07	0.28	−0.45	0.16	−0.26	0.04	0.96	0.15	0.59
	QR	0.19	0.31	0.07	0.59	0.16	0.56	0.02	0.99	0.12	0.69
	ALL	0.19	0.3	0.25	0.05	0.15	0.24	0.03	0.97	0.13	0.67
OSAVI	AC	0.12	0.52	0.24	0.27	0.16	0.15	0.02	0.99	0.11	0.83
	FR	0.03	0.96	0.15	0.61	0.2	0.29	0.02	0.99	0.13	0.73
	PL	0.23	0.34	0.27	−0.28	0.23	0	0.04	0.99	0.17	0.78
	QR	0.17	0.64	0.06	0.39	0.15	0.24	0.04	0.97	0.11	0.76
	ALL	0.19	0.69	0.21	0.18	0.19	0.24	0.04	0.99	0.13	0.8
MCARI	AC	0.12	0.31	0.24	0.23	0.12	0.11	0.03	0.97	0.10	0.7
	FR	0.04	0.84	0.10	0.58	0.10	0.4	0.01	1	0.07	0.79
	PL	0.17	0.20	0.25	−0.39	0.12	0	0.04	0.97	0.12	0.67
	QR	0.15	0.53	0.04	0.53	0.09	0.32	0.02	0.98	0.09	0.68
	ALL	0.15	0.57	0.2	−0.02	0.11	0.28	0.03	0.98	0.10	0.7

Table A3. Pearson correlation coefficient (r) and root mean square error (RMSE) by vegetation index and extraction window (as well as all windows) for each tree species and all species for the 50% matching method.

VI	SP	Window 1		Window 2		Window 3		Window 4		All Windows	
		RMSE	r	RMSE	r	RMSE	r	RMSE	r	RMSE	r
NDVI	AC	0.07	0.66	0.08	0.31	0.11	0.23	0.06	0.81	0.07	0.74
	FR	0.02	0.91	0.12	0.48	0.17	0.27	0.09	0.86	0.12	0.6
	PL	0.15	0.12	0.14	−0.22	0.17	−0.05	0.06	0.93	0.12	0.66
	QR	0.09	0.71	0.04	0.35	0.11	0.33	0.1	0.82	0.10	0.59
	ALL	0.12	0.65	0.10	0.23	0.15	0.1	0.07	0.88	0.10	0.66
ARVI	AC	0.08	0.71	0.10	0.37	0.15	0.24	0.08	0.79	0.09	0.72
	FR	0.03	0.90	0.15	0.36	0.19	0.34	0.11	0.8	0.14	0.58
	PL	0.17	0.27	0.18	−0.2	0.19	0.09	0.07	0.91	0.13	0.65
	QR	0.11	0.70	0.04	0.86	0.14	0.39	0.11	0.79	0.11	0.58
	ALL	0.13	0.68	0.13	0.19	0.17	0.18	0.09	0.86	0.12	0.66
NGBDI	AC	0.14	0.46	0.2	0.27	0.11	0.47	0.07	0.72	0.11	0.57
	FR	0.09	0.70	0.14	0.23	0.07	0.49	0.04	0.83	0.08	0.58
	PL	0.18	0.24	0.17	0.01	0.11	−0.18	0.08	0.75	0.13	0.41
	QR	0.14	0.10	0.06	0.63	0.09	0.47	0.04	0.87	0.09	0.52
	ALL	0.16	0.24	0.17	0.08	0.09	0.3	0.06	0.76	0.10	0.48
RGBVI	AC	0.27	0.44	0.31	0.51	0.23	0.29	0.09	0.77	0.17	0.59
	FR	0.13	0.57	0.21	0.24	0.12	0.42	0.06	0.87	0.12	0.63
	PL	0.30	0.09	0.29	−0.47	0.17	−0.32	0.09	0.77	0.21	0.41
	QR	0.27	0.04	0.08	0.48	0.17	0.48	0.06	0.89	0.17	0.48
	ALL	0.28	0.12	0.27	0	0.17	0.16	0.08	0.8	0.18	0.49
OSAVI	AC	0.16	0.22	0.24	0.28	0.18	0.05	0.08	0.87	0.13	0.69
	FR	0.06	0.81	0.15	0.58	0.23	0.25	0.14	0.88	0.17	0.66
	PL	0.31	0.18	0.27	−0.31	0.23	−0.06	0.11	0.92	0.22	0.65
	QR	0.22	0.44	0.06	0.35	0.17	0.18	0.15	0.80	0.17	0.49
	ALL	0.25	0.54	0.21	0.15	0.21	0.14	0.11	0.88	0.18	0.63
MCARI	AC	0.17	0.35	0.24	0.33	0.14	−0.01	0.05	0.86	0.12	0.57
	FR	0.06	0.70	0.10	0.59	0.12	0.29	0.06	0.91	0.09	0.68
	PL	0.23	0.16	0.26	−0.40	0.12	−0.06	0.07	0.87	0.16	0.52
	QR	0.20	0.21	0.04	0.32	0.09	0.31	0.07	0.89	0.13	0.42
	ALL	0.20	0.37	0.20	0.01	0.12	0.15	0.06	0.88	0.13	0.52

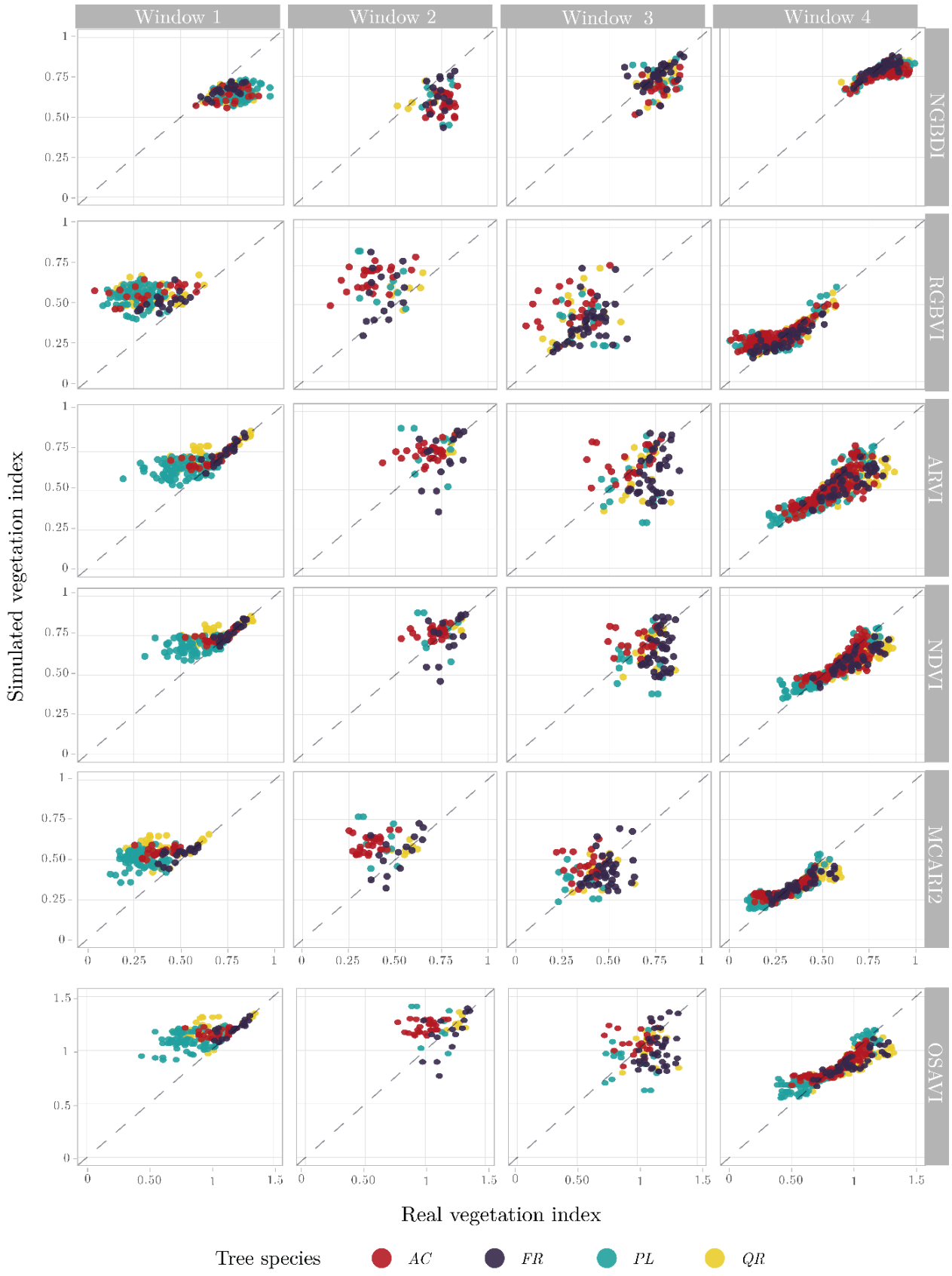

Figure A3. Scatter plots of real and simulated vegetation indices (NGBDI, RGBVI, ARVI, NDVI, MCARI2, and OSAVI) for Sentinel-2 values by size of the extraction window for the 50% matching method. Colors correspond to the four tree species studied.

Table A4. Pearson correlation coefficient (r) and root mean square error (RMSE) by vegetation index and extraction window (as well as all windows) as a function of the day of the year in 2021 (DOY) (as well as all DOYs) for the 10% matching method.

VI	DOY	Window 1		Window 2		Window 3		Window 4		All Windows	
		RMSE	r	RMSE	r	RMSE	r	RMSE	r	RMSE	r
NDVI	156	0.07	0.87	0.07	0.53	0.12	0.24	0.02	0.99	0.06	0.88
	166	0.09	0.79	0.08	0.43	0.16	0	0.02	0.99	0.08	0.83
	201	0.10	0.82	0.12	0.28	0.13	−0.03	0.02	0.99	0.08	0.83
	226	0.09	0.82	0.10	0.31	0.14	0.18	0.02	0.99	0.07	0.83
	248	0.07	0.81	0.11	−0.16	0.10	0.37	0.01	0.99	0.06	0.86
	ALL	0.08	0.82	0.10	0.28	0.13	0.17	0.02	0.99	0.07	0.84
ARVI	156	0.08	0.88	0.08	0.53	0.14	0.43	0.02	0.99	0.07	0.86
	166	0.09	0.83	0.09	0.39	0.17	0.17	0.02	0.99	0.08	0.83
	201	0.11	0.83	0.15	0.22	0.16	0.09	0.02	0.99	0.09	0.81
	226	0.09	0.85	0.13	0.27	0.16	0.20	0.02	0.99	0.09	0.82
	248	0.07	0.87	0.15	−0.29	0.11	0.52	0.02	0.99	0.07	0.88
	ALL	0.09	0.84	0.12	0.23	0.15	0.27	0.02	0.99	0.08	0.84
NGBDI	156	0.08	0.66	0.15	−0.09	0.09	0.32	0.02	0.97	0.07	0.73
	166	0.08	0.73	0.13	0.26	0.09	0.08	0.02	0.97	0.06	0.77
	201	0.10	0.41	0.17	0.12	0.06	0.42	0.03	0.94	0.08	0.63
	226	0.09	0.36	0.18	−0.12	0.09	0.32	0.02	0.94	0.08	0.65
	248	0.08	0.30	0.17	−0.11	0.08	0.32	0.02	0.95	0.07	0.64
	ALL	0.09	0.57	0.16	0.11	0.08	0.40	0.02	0.96	0.072	0.7
RGBVI	156	0.19	0.33	0.21	0.12	0.15	0.10	0.03	0.98	0.13	0.71
	166	0.18	0.40	0.22	−0.01	0.13	0.31	0.03	0.97	0.12	0.71
	201	0.21	0.19	0.26	0.12	0.14	0.03	0.04	0.94	0.14	0.6
	226	0.21	0.20	0.28	−0.11	0.18	0.13	0.03	0.97	0.15	0.63
	248	0.18	0.20	0.3	−0.37	0.14	0.13	0.03	0.96	0.13	0.61
	ALL	0.19	0.30	0.25	0.05	0.15	0.24	0.03	0.97	0.13	0.67
OSAVI	156	0.15	0.79	0.13	0.51	0.18	0.43	0.03	0.99	0.11	0.85
	166	0.18	0.67	0.15	0.35	0.24	0.08	0.04	0.99	0.13	0.8
	201	0.22	0.68	0.24	0.07	0.17	0.11	0.04	0.99	0.14	0.79
	226	0.21	0.70	0.26	0.42	0.2	0.16	0.04	0.98	0.15	0.77
	248	0.18	0.61	0.24	−0.70	0.14	0.28	0.03	0.99	0.12	0.81
	ALL	0.19	0.69	0.21	0.18	0.19	0.24	0.04	0.99	0.13	0.8
MCARI	156	0.12	0.68	0.14	0.32	0.10	0.33	0.02	0.99	0.08	0.78
	166	0.13	0.59	0.14	0.33	0.13	0.13	0.03	0.98	0.09	0.73
	201	0.16	0.59	0.21	−0.20	0.08	0.40	0.03	0.97	0.11	0.68
	226	0.17	0.55	0.25	0	0.13	0.13	0.03	0.97	0.12	0.66
	248	0.16	0.45	0.22	−0.76	0.07	0.31	0.03	0.96	0.10	0.68
	ALL	0.15	0.57	0.2	−0.02	0.11	0.28	0.03	0.98	0.10	0.7

Table A5. Pearson correlation coefficient (r) and root mean square error (RMSE) by vegetation index and extraction window (as well as all windows) as a function of the day of the year in 2021 (DOY) (as well as all DOYs) for the 50% matching method.

VI	DOY	Window 1		Window 2		Window 3		Window 4		All Windows	
		RMSE	r	RMSE	r	RMSE	r	RMSE	r	RMSE	r
NDVI	156	0.11	0.72	0.07	0.46	0.14	0.23	0.07	0.9	0.09	0.72
	166	0.11	0.65	0.09	0.27	0.17	−0.06	0.08	0.87	0.10	0.67
	201	0.14	0.60	0.13	0.23	0.14	−0.03	0.07	0.9	0.11	0.64
	226	0.12	0.70	0.11	0.3	0.15	0.10	0.07	0.88	0.10	0.64
	248	0.11	0.66	0.11	−0.32	0.13	0.18	0.07	0.86	0.09	0.66
	ALL	0.12	0.65	0.1	0.23	0.15	0.10	0.07	0.88	0.10	0.66

Table A5. *Cont.*

VI	DOY	Window 1		Window 2		Window 3		Window 4		All Windows	
		RMSE	r	RMSE	r	RMSE	r	RMSE	r	RMSE	r
ARVI	156	0.12	0.75	0.09	0.54	0.16	0.36	0.09	0.86	0.11	0.7
	166	0.13	0.67	0.1	0.26	0.19	0.06	0.08	0.86	0.11	0.67
	201	0.16	0.64	0.16	0.13	0.17	0.06	0.08	0.89	0.12	0.64
	226	0.14	0.69	0.13	0.27	0.19	0.07	0.08	0.89	0.12	0.64
	248	0.11	0.70	0.16	−0.34	0.15	0.35	0.10	0.80	0.11	0.64
	ALL	0.13	0.68	0.13	0.19	0.17	0.18	0.09	0.86	0.12	0.66
NGBDI	156	0.15	0.41	0.16	−0.19	0.09	0.22	0.06	0.81	0.11	0.54
	166	0.14	0.31	0.14	0.12	0.09	0.02	0.06	0.87	0.10	0.52
	201	0.17	0.10	0.17	0.10	0.08	0.23	0.07	0.57	0.12	0.36
	226	0.16	−0.08	0.18	−0.12	0.1	0.23	0.07	0.64	0.11	0.43
	248	0.15	0.09	0.17	−0.07	0.09	0.20	0.06	0.66	0.10	0.44
	ALL	0.16	0.24	0.17	0.08	0.09	0.30	0.06	0.76	0.10	0.48
RGBVI	156	0.27	0.27	0.24	0.04	0.17	0.02	0.08	0.86	0.17	0.55
	166	0.25	0.06	0.25	−0.32	0.14	0.19	0.08	0.85	0.16	0.52
	201	0.30	0.09	0.27	0.10	0.15	0.02	0.09	0.62	0.19	0.41
	226	0.29	−0.12	0.28	−0.07	0.21	0.09	0.08	0.77	0.19	0.47
	248	0.26	0.2	0.3	−0.36	0.16	0.10	0.08	0.73	0.17	0.43
	ALL	0.28	0.12	0.27	0	0.17	0.16	0.08	0.80	0.18	0.49
OSAVI	156	0.20	0.68	0.13	0.47	0.20	0.32	0.12	0.91	0.16	0.70
	166	0.23	0.54	0.16	0.25	0.25	0	0.12	0.87	0.18	0.62
	201	0.28	0.53	0.25	0.03	0.20	−0.07	0.12	0.87	0.19	0.59
	226	0.28	0.56	0.26	0.42	0.23	0.06	0.11	0.88	0.20	0.6
	248	0.25	0.45	0.24	−0.72	0.15	0.14	0.09	0.88	0.16	0.64
	ALL	0.25	0.54	0.21	0.15	0.21	0.14	0.11	0.88	0.18	0.63
MCARI	156	0.17	0.49	0.15	0.34	0.12	0.15	0.06	0.91	0.12	0.59
	166	0.18	0.39	0.15	0.26	0.13	0.11	0.06	0.9	0.12	0.55
	201	0.22	0.34	0.21	−0.21	0.10	0.18	0.07	0.85	0.14	0.47
	226	0.22	0.33	0.26	0.10	0.15	0.01	0.07	0.86	0.15	0.48
	248	0.21	0.34	0.23	−0.77	0.09	0.14	0.06	0.81	0.13	0.51
	ALL	0.20	0.37	0.20	0.01	0.12	0.15	0.06	0.88	0.13	0.52

References

1. Xu, F.; Yan, J.; Heremans, S.; Somers, B. Pan-European urban green space dynamics: A view from space between 1990 and 2015. *Landsc. Urban Plan.* **2022**, *226*, 104477. [CrossRef]
2. Andersson-Sköld, Y.; Thorsson, S.; Rayner, D.; Lindberg, F.; Janhäll, S.; Jonsson, A.; Moback, U.; Bergman, R.; Granberg, M. An integrated method for assessing climate-related risks and adaptation alternatives in urban areas. *Clim. Risk Manag.* **2015**, *7*, 31–50. [CrossRef]
3. Bolund, P.; Hunhammar, S. Ecosystem services in urban areas. *Ecol. Econ.* **1999**, *29*, 293–301. [CrossRef]
4. Nowak, D.J.; Crane, D.E. Carbon storage and sequestration by urban trees in the USA. *Environ. Pollut.* **2002**, *116*, 381–389. [CrossRef] [PubMed]
5. Andersson, E.; Barthel, S.; Ahrné, K. Measuring Social–Ecological Dynamics Behind the Generation of Ecosystem Services. *Ecol. Appl.* **2007**, *17*, 1267–1278. [CrossRef]
6. Wolf, K.L.; Lam, S.T.; McKeen, J.K.; Richardson, G.R.A.; van den Bosch, M.; Bardekjian, A.C. Urban Trees and Human Health: A Scoping Review. *Int. J. Environ. Res. Public Health* **2020**, *17*, 4371. [CrossRef]
7. Czaja, M.; Kołton, A.; Muras, P. The Complex Issue of Urban Trees—Stress Factor Accumulation and Ecological Service Possibilities. *Forests* **2020**, *11*, 932. [CrossRef]
8. Sæbø, A.; Borzan, Ž.; Ducatillion, C.; Hatzistathis, A.; Lagerström, T.; Supuka, J.; García-Valdecantos, J.L.; Rego, F.; Van Slycken, J. The Selection of Plant Materials for Street Trees, Park Trees and Urban Woodland. In *Urban Forests and Trees: A Reference Book*; Konijnendijk, C., Nilsson, K., Randrup, T., Schipperijn, J., Eds.; Springer: Berlin/Heidelberg, Germany, 2005; pp. 257–280. ISBN 978-3-540-27684-5.
9. Ma, B.; Hauer, R.J.; Östberg, J.; Koeser, A.K.; Wei, H.; Xu, C. A global basis of urban tree inventories: What comes first the inventory or the program. *Urban For. Urban Green.* **2021**, *60*, 127087. [CrossRef]
10. Hilbert, D.; Roman, L.; Koeser, A.; Vogt, J.; van Doorn, N. Urban Tree Mortality: A Literature Review. *Arboric. Urban For.* **2019**, *45*, 167–200. [CrossRef]

11. Shahtahmassebi, A.R.; Li, C.; Fan, Y.; Wu, Y.; Lin, Y.; Gan, M.; Wang, K.; Malik, A.; Blackburn, G.A. Remote sensing of urban green spaces: A review. *Urban For. Urban Green.* **2021**, *57*, 126946. [CrossRef]
12. Velasquez-Camacho, L.; Cardil, A.; Mohan, M.; Etxegarai, M.; Anzaldi, G.; de-Miguel, S. Remotely Sensed Tree Characterization in Urban Areas: A Review. *Remote Sens.* **2021**, *13*, 4889. [CrossRef]
13. Jia, W.; Zhao, S.; Zhang, X.; Liu, S.; Henebry, G.M.; Liu, L. Urbanization imprint on land surface phenology: The urban–rural gradient analysis for Chinese cities. *Glob. Chang. Biol.* **2021**, *27*, 2895–2904. [CrossRef] [PubMed]
14. Hu, M.; Li, X.; Xu, Y.; Huang, Z.; Chen, C.; Chen, J.; Du, H. Remote sensing monitoring of the spatiotemporal dynamics of urban forest phenology and its response to climate and urbanization. *Urban Clim.* **2024**, *53*, 101810. [CrossRef]
15. Zhang, Y.; Yin, P.; Li, X.; Niu, Q.; Wang, Y.; Cao, W.; Huang, J.; Chen, H.; Yao, X.; Yu, L.; et al. The divergent response of vegetation phenology to urbanization: A case study of Beijing city, China. *Sci. Total Environ.* **2022**, *803*, 150079. [CrossRef] [PubMed]
16. Zhou, J.; Jia, L.; Menenti, M.; Gorte, B. On the performance of remote sensing time series reconstruction methods—A spatial comparison. *Remote Sens. Environ.* **2016**, *187*, 367–384. [CrossRef]
17. Chang, M.-E.; Zhao, Z.-Q.; Chang, H.-T.; Shu, B. Urban green infrastructure health assessment, based on landsat 8 remote sensing and entropy landscape metrics. *Eur. J. Remote Sens.* **2021**, *54*, 417–430. [CrossRef]
18. Li, L.; Zhou, X.; Chen, L.; Chen, L.; Zhang, Y.; Liu, Y. Estimating Urban Vegetation Biomass from Sentinel-2A Image Data. *Forests* **2020**, *11*, 125. [CrossRef]
19. Degerickx, J.; Roberts, D.A.; McFadden, J.P.; Hermy, M.; Somers, B. Urban tree health assessment using airborne hyperspectral and LiDAR imagery. *Int. J. Appl. Earth Obs. Geoinf.* **2018**, *73*, 26–38. [CrossRef]
20. Näsi, R.; Honkavaara, E.; Blomqvist, M.; Lyytikäinen-Saarenmaa, P.; Hakala, T.; Viljanen, N.; Kantola, T.; Holopainen, M. Remote sensing of bark beetle damage in urban forests at individual tree level using a novel hyperspectral camera from UAV and aircraft. *Urban For. Urban Green.* **2018**, *30*, 72–83. [CrossRef]
21. Granero-Belinchon, C.; Adeline, K.; Lemonsu, A.; Briottet, X. Phenological Dynamics Characterization of Alignment Trees with Sentinel-2 Imagery: A Vegetation Indices Time Series Reconstruction Methodology Adapted to Urban Areas. *Remote Sens.* **2020**, *12*, 639. [CrossRef]
22. Leisenheimer, L.; Wellmann, T.; Jänicke, C.; Haase, D. Monitoring drought impacts on street trees using remote sensing—Disentangling temporal and species-specific response patterns with Sentinel-2 imagery. *Ecol. Inform.* **2024**, *82*, 102659. [CrossRef]
23. Lausch, A.; Erasmi, S.; King, D.J.; Magdon, P.; Heurich, M. Understanding Forest Health with Remote Sensing -Part I—A Review of Spectral Traits, Processes and Remote-Sensing Characteristics. *Remote Sens.* **2016**, *8*, 1029. [CrossRef]
24. Houborg, R.; Fisher, J.B.; Skidmore, A.K. Advances in remote sensing of vegetation function and traits. *Int. J. Appl. Earth Obs. Geoinf.* **2015**, *43*, 1–6. [CrossRef]
25. Padalia, H.; Sinha, S.K.; Bhave, V.; Trivedi, N.K.; Senthil Kumar, A. Estimating canopy LAI and chlorophyll of tropical forest plantation (North India) using Sentinel-2 data. *Adv. Space Res.* **2020**, *65*, 458–469. [CrossRef]
26. Miraglio, T.; Adeline, K.; Huesca, M.; Ustin, S.; Briottet, X. Assessing vegetation traits estimates accuracies from the future SBG and biodiversity hyperspectral missions over two Mediterranean Forests. *Int. J. Remote Sens.* **2022**, *43*, 3537–3562. [CrossRef]
27. Croft, H.; Chen, J.M.; Luo, X.; Bartlett, P.; Chen, B.; Staebler, R.M. Leaf chlorophyll content as a proxy for leaf photosynthetic capacity. *Glob. Chang. Biol.* **2017**, *23*, 3513–3524. [CrossRef]
28. Filella, I.; Penuelas, J. The red edge position and shape as indicators of plant chlorophyll content, biomass and hydric status. *Int. J. Remote Sens.* **1994**, *15*, 1459–1470. [CrossRef]
29. Massacci, A.; Lannelli, M.A.; Pietrini, F.; Loreto, F. The effect of growth at low temperature on photosynthetic characteristics and mechanisms of photoprotection of maize leaves. *J. Exp. Bot.* **1995**, *46*, 119–127. [CrossRef]
30. Talebzadeh, F.; Valeo, C. Evaluating the Effects of Environmental Stress on Leaf Chlorophyll Content as an Index for Tree Health. *IOP Conf. Ser. Earth Environ. Sci.* **2022**, *1006*, 012007. [CrossRef]
31. Colombo, R.; Busetto, L.; Meroni, M.; Rossini, M.; Panigada, C. Optical Remote Sensing of Vegetation Water Content. In *Hyperspectral Indices and Image Classifications for Agriculture and Vegetation*; CRC Press: Boca Raton, FL, USA, 2018; ISBN 978-1-315-15933-1.
32. Gara, T.W.; Rahimzadeh-Bajgiran, P.; Darvishzadeh, R. Forest Leaf Mass per Area (LMA) through the Eye of Optical Remote Sensing: A Review and Future Outlook. *Remote Sens.* **2021**, *13*, 3352. [CrossRef]
33. Jacquemoud, S.; Ustin, S. *Leaf Optical Properties*; Cambridge University Press: Cambridge, UK, 2019; ISBN 978-1-108-48126-7.
34. Peñuelas, J.; Rutishauser, T.; Filella, I. Phenology Feedbacks on Climate Change. *Science* **2009**, *324*, 887–888. [CrossRef] [PubMed]
35. Duncan, W.G. Leaf Angles, Leaf Area, and Canopy Photosynthesis1. *Crop Sci.* **1971**, *11*, 482–485. [CrossRef]
36. Sinoquet, H.; Stephan, J.; Sonohat, G.; Lauri, P.É.; Monney, P. Simple equations to estimate light interception by isolated trees from canopy structure features: Assessment with three-dimensional digitized apple trees. *New Phytol.* **2007**, *175*, 94–106. [CrossRef] [PubMed]
37. Helsen, K.; Bassi, L.; Feilhauer, H.; Kattenborn, T.; Matsushima, H.; Van Cleemput, E.; Somers, B.; Honnay, O. Evaluating different methods for retrieving intraspecific leaf trait variation from hyperspectral leaf reflectance. *Ecol. Indic.* **2021**, *130*, 108111. [CrossRef]
38. Granero-Belinchon, C.; Adeline, K.; Briottet, X. Impact of the number of dates and their sampling on a NDVI time series reconstruction methodology to monitor urban trees with Venμs satellite. *Int. J. Appl. Earth Obs. Geoinform.* **2021**, *95*, 102257. [CrossRef]
39. Zhen, J.; Jiang, X.; Xu, Y.; Miao, J.; Zhao, D.; Wang, J.; Wang, J.; Wu, G. Mapping leaf chlorophyll content of mangrove forests with Sentinel-2 images of four periods. *Int. J. Appl. Earth Obs. Geoinform.* **2021**, *102*, 102387. [CrossRef]

40. Li, Y.; Ma, Q.; Chen, J.M.; Croft, H.; Luo, X.; Zheng, T.; Rogers, C.; Liu, J. Fine-scale leaf chlorophyll distribution across a deciduous forest through two-step model inversion from Sentinel-2 data. *Remote Sens. Environ.* **2021**, *264*, 112618. [CrossRef]
41. Clevers, J.G.P.W.; Kooistra, L.; Van den Brande, M.M.M. Using Sentinel-2 Data for Retrieving LAI and Leaf and Canopy Chlorophyll Content of a Potato Crop. *Remote Sens.* **2017**, *9*, 405. [CrossRef]
42. Qian, B.; Ye, H.; Huang, W.; Xie, Q.; Pan, Y.; Xing, N.; Ren, Y.; Guo, A.; Jiao, Q.; Lan, Y. A sentinel-2-based triangular vegetation index for chlorophyll content estimation. *Agric. For. Meteorol.* **2022**, *322*, 109000. [CrossRef]
43. Wu, C.; Niu, Z.; Tang, Q.; Huang, W. Estimating chlorophyll content from hyperspectral vegetation indices: Modeling and validation. *Agric. For. Meteorol.* **2008**, *148*, 1230–1241. [CrossRef]
44. Pasqualotto, N.; Delegido, J.; Van Wittenberghe, S.; Rinaldi, M.; Moreno, J. Multi-Crop Green LAI Estimation with a New Simple Sentinel-2 LAI Index (SeLI). *Sensors* **2019**, *19*, 904. [CrossRef] [PubMed]
45. Miao, J.; Wang, J.; Zhao, D.; Shen, Z.; Xiang, H.; Gao, C.; Li, W.; Cui, L.; Wu, G. Modeling strategies and influencing factors in retrieving canopy equivalent water thickness of mangrove forest with Sentinel-2 image. *Ecol. Indic.* **2024**, *158*, 111497. [CrossRef]
46. Zhou, T.; Fu, H.; Sun, C.; Wang, S. Shadow Detection and Compensation from Remote Sensing Images under Complex Urban Conditions. *Remote Sens.* **2021**, *13*, 699. [CrossRef]
47. Jilge, M.; Heiden, U.; Neumann, C.; Feilhauer, H. Gradients in urban material composition: A new concept to map cities with spaceborne imaging spectroscopy data. *Remote Sens. Environ.* **2019**, *223*, 179–193. [CrossRef]
48. Kotthaus, S.; Smith, T.E.L.; Wooster, M.J.; Grimmond, C.S.B. Derivation of an urban materials spectral library through emittance and reflectance spectroscopy. *ISPRS J. Photogramm. Remote Sens.* **2014**, *94*, 194–212. [CrossRef]
49. Kaufman, Y.J.; Tanre, D. Atmospherically Resistant Vegetation Index (ARVI) for EOS-MODIS. *IEEE Trans. Geosci. Remote Sens.* **1992**, *30*, 261–270. [CrossRef]
50. Rondeaux, G.; Steven, M.; Baret, F. Optimization of soil-adjusted vegetation indices. *Remote Sens. Environ.* **1996**, *55*, 95–107. [CrossRef]
51. De Castro Oliveira, J.; Féret, J.-B.; Ponzoni, F.J.; Nouvellon, Y.; Gastellu-Etchegorry, J.-P.; Campoe, O.C.; Stape, J.L.; Rodriguez, L.C.E.; le Maire, G. Simulating the Canopy Reflectance of Different Eucalypt Genotypes With the DART 3-D Model. *IEEE J. Sel. Top. Appl. Earth Obs. Remote Sens.* **2017**, *10*, 4844–4852. [CrossRef]
52. Morcillo-Pallarés, P.; Rivera-Caicedo, J.P.; Belda, S.; De Grave, C.; Burriel, H.; Moreno, J.; Verrelst, J. Quantifying the Robustness of Vegetation Indices through Global Sensitivity Analysis of Homogeneous and Forest Leaf-Canopy Radiative Transfer Models. *Remote Sens.* **2019**, *11*, 2418. [CrossRef]
53. Xiao, Y.; Zhao, W.; Zhou, D.; Gong, H. Sensitivity Analysis of Vegetation Reflectance to Biochemical and Biophysical Variables at Leaf, Canopy, and Regional Scales. *IEEE Trans. Geosci. Remote Sens.* **2014**, *52*, 4014–4024. [CrossRef]
54. Gu, C.; Du, H.; Mao, F.; Han, N.; Zhou, G.; Xu, X.; Sun, S.; Gao, G. Global sensitivity analysis of PROSAIL model parameters when simulating Moso bamboo forest canopy reflectance. *Int. J. Remote Sens.* **2016**, *37*, 5270–5286. [CrossRef]
55. Wang, Y.; Kallel, A.; Yang, X.; Regaieg, O.; Lauret, N.; Guilleux, J.; Chavanon, E.; Gastellu-Etchegorry, J.-P. DART-Lux: An unbiased and rapid Monte Carlo radiative transfer method for simulating remote sensing images. *Remote Sens. Environ.* **2022**, *274*, 112973. [CrossRef]
56. Widlowski, J.-L.; Mio, C.; Disney, M.; Adams, J.; Andredakis, I.; Atzberger, C.; Brennan, J.; Busetto, L.; Chelle, M.; Ceccherini, G.; et al. The fourth phase of the radiative transfer model intercomparison (RAMI) exercise: Actual canopy scenarios and conformity testing. *Remote Sens. Environ.* **2015**, *169*, 418–437. [CrossRef]
57. Zhen, Z.; Benromdhane, N.; Kallel, A.; Wang, Y.; Regaieg, O.; Boitard, P.; Landier, L.; Chavanon, E.; Lauret, N.; Guilleux, J.; et al. DART: A 3D radiative transfer model for urban studies. In Proceedings of the 2023 Joint Urban Remote Sensing Event (JURSE), Herklion, Greece, 17–19 May 2023.
58. Stewart, I.D.; Oke, T.R. Local Climate Zones for Urban Temperature Studies. *Bull. Am. Meteorol. Soc.* **2012**, *93*, 1879–1900. [CrossRef]
59. Aslam, A.; Rana, I.A. The use of local climate zones in the urban environment: A systematic review of data sources, methods, and themes. *Urban Clim.* **2022**, *42*, 101120. [CrossRef]
60. Zhao, C.; Weng, Q.; Wang, Y.; Hu, Z.; Wu, C. Use of local climate zones to assess the spatiotemporal variations of urban vegetation phenology in Austin, Texas, USA. *GIScience Remote Sens.* **2022**, *59*, 393–409. [CrossRef]
61. Demuzere, M.; Bechtel, B.; Middel, A.; Mills, G. Mapping Europe into local climate zones. *PLoS ONE* **2019**, *14*, e0214474. [CrossRef]
62. Gascon, F.; Gastellu-Etchegorry, J.-P.; Lefevre-Fonollosa, M.-J.; Dufrene, E. Retrieval of forest biophysical variables by inverting a 3-D radiative transfer model and using high and very high resolution imagery. *Int. J. Remote Sens.* **2004**, *25*, 5601–5616. [CrossRef]
63. Gastellu-Etchegorry, J.-P.; Yin, T.; Lauret, N.; Cajgfinger, T.; Gregoire, T.; Grau, E.; Feret, J.-B.; Lopes, M.; Guilleux, J.; Dedieu, G.; et al. Discrete Anisotropic Radiative Transfer (DART 5) for Modeling Airborne and Satellite Spectroradiometer and LIDAR Acquisitions of Natural and Urban Landscapes. *Remote Sens.* **2015**, *7*, 1667–1701. [CrossRef]
64. Gastellu-Etchegorry, J.P.; Demarez, V.; Pinel, V.; Zagolski, F. Modeling radiative transfer in heterogeneous 3-D vegetation canopies. *Remote Sens. Environ.* **1996**, *58*, 131–156. [CrossRef]
65. Féret, J.-B.; Gitelson, A.A.; Noble, S.D.; Jacquemoud, S. PROSPECT-D: Towards modeling leaf optical properties through a complete lifecycle. *Remote Sens. Environ.* **2017**, *193*, 204–215. [CrossRef]

66. Feret, J.-B.; François, C.; Asner, G.P.; Gitelson, A.A.; Martin, R.E.; Bidel, L.P.R.; Ustin, S.L.; le Maire, G.; Jacquemoud, S. PROSPECT-4 and 5: Advances in the leaf optical properties model separating photosynthetic pigments. *Remote Sens. Environ.* **2008**, *112*, 3030–3043. [CrossRef]
67. Miraglio, T.; Huesca, M.; Gastellu-Etchegorry, J.-P.; Schaaf, C.; Adeline, K.R.M.; Ustin, S.L.; Briottet, X. Impact of Modeling Abstractions When Estimating Leaf Mass per Area and Equivalent Water Thickness over Sparse Forests Using a Hybrid Method. *Remote Sens.* **2021**, *13*, 3235. [CrossRef]
68. Gaubert, T.; Adeline, K.; Huesca, M.; Ustin, S.; Briottet, X. Estimation of Oak Leaf Functional Traits for California Woodland Savannas and Mixed Forests: Comparison between Statistical, Physical, and Hybrid Methods Using Spectroscopy. *Remote Sens.* **2024**, *16*, 29. [CrossRef]
69. Lacherade, S.; Miesch, C.; Briottet, X.; Le Men, H. Spectral variability and bidirectional reflectance behaviour of urban materials at a 20 cm spatial resolution in the visible and near-infrared wavelengths. A case study over Toulouse (France). *Int. J. Remote Sens.* **2005**, *26*, 3859–3866. [CrossRef]
70. Baudin, M.; Dutfoy, A.; Iooss, B.; Popelin, A.-L. OpenTURNS: An Industrial Software for Uncertainty Quantification in Simulation. In *Handbook of Uncertainty Quantification*; Ghanem, R., Higdon, D., Owhadi, H., Eds.; Springer International Publishing: Cham, Switzerland, 2017; pp. 2001–2038; ISBN 978-3-319-12385-1.
71. ESA. *Sentinel-2 Annual Performance Report—Year 2022*; European Space Agency (ESA): Paris, France, 2022.
72. Richardson, A.J.; Wiegand, C.L. Distinguishing vegetation from soil background information. *Photogramm. Eng. Remote Sens.* **1977**, *43*, 1541–1552.
73. Louhaichi, M.; Borman, M.M.; Johnson, D.E. Spatially Located Platform and Aerial Photography for Documentation of Grazing Impacts on Wheat. *Geocarto Int.* **2001**, *16*, 65–70. [CrossRef]
74. Woebbecke, D.M.; Meyer, G.E.; Von Bargen, K.; Mortensen, D.A. Color Indices for Weed Identification Under Various Soil, Residue, and Lighting Conditions. *Trans. ASAE* **1995**, *38*, 259–269. [CrossRef]
75. Gitelson, A.A.; Kaufman, Y.J.; Stark, R.; Rundquist, D. Novel algorithms for remote estimation of vegetation fraction. *Remote Sens. Environ.* **2002**, *80*, 76–87. [CrossRef]
76. Bendig, J.; Yu, K.; Aasen, H.; Bolten, A.; Bennertz, S.; Broscheit, J.; Gnyp, M.L.; Bareth, G. Combining UAV-based plant height from crop surface models, visible, and near infrared vegetation indices for biomass monitoring in barley. *Int. J. Appl. Earth Obs. Geoinformation* **2015**, *39*, 79–87. [CrossRef]
77. Rouse, J.W.; Haas, R.H.; Schell, J.A.; Deering, D.W. Monitoring vegetation systems. In *The Great Plains with ERTS*; NASA Special Publications: Washington, DC, USA, 1974.
78. Gitelson, A.; Merzlyak, M.N. Quantitative estimation of chlorophyll-a using reflectance spectra: Experiments with autumn chestnut and maple leaves. *J. Photochem. Photobiol. B Biol.* **1994**, *22*, 247–252. [CrossRef]
79. Haboudane, D.; Miller, J.R.; Pattey, E.; Zarco-Tejada, P.J.; Strachan, I.B. Hyperspectral vegetation indices and novel algorithms for predicting green LAI of crop canopies: Modeling and validation in the context of precision agriculture. *Remote Sens. Environ.* **2004**, *90*, 337–352. [CrossRef]
80. Haboudane, D.; Miller, J.R.; Tremblay, N.; Zarco-Tejada, P.J.; Dextraze, L. Integrated narrow-band vegetation indices for prediction of crop chlorophyll content for application to precision agriculture. *Remote Sens. Environ.* **2002**, *81*, 416–426. [CrossRef]
81. Huang, W.; Wang, Z.; Huang, L.; Lamb, D.W.; Ma, Z.; Zhang, J.; Wang, J.; Zhao, C. Estimation of vertical distribution of chlorophyll concentration by bi-directional canopy reflectance spectra in winter wheat. *Precis. Agric.* **2011**, *12*, 165–178. [CrossRef]
82. Iooss, B.; Lemaître, P. A Review on Global Sensitivity Analysis Methods. In *Uncertainty Management in Simulation-Optimization of Complex Systems: Algorithms and Applications*; Dellino, G., Meloni, C., Eds.; Operations Research/Computer Science Interfaces Series; Springer: Boston, MA, USA, 2015; pp. 101–122; ISBN 978-1-4899-7547-8.
83. Le Gratiet, L.; Marelli, S.; Sudret, B. Metamodel-Based Sensitivity Analysis: Polynomial Chaos Expansions and Gaussian Processes. In *Handbook of Uncertainty Quantification*; Springer: Berlin/Heidelberg, Germany, 2017; pp. 1289–1325.
84. Saltelli, A. Making best use of model evaluations to compute sensitivity indices. *Comput. Phys. Commun.* **2002**, *145*, 280–297. [CrossRef]
85. INSEE (French National Institute of Statistics and Economic Studies). *Population Census 2020*; INSEE: Paris, France, 2022.
86. Scheffler, D.; Hollstein, A.; Diedrich, H.; Segl, K.; Hostert, P. AROSICS: An Automated and Robust Open-Source Image Co-Registration Software for Multi-Sensor Satellite Data. *Remote Sens.* **2017**, *9*, 676. [CrossRef]
87. Wei, S.; Yin, T.; Dissegna, M.A.; Whittle, A.J.; Ow, G.L.F.; Yusof, M.L.M.; Lauret, N.; Gastellu-Etchegorry, J.-P. An assessment study of three indirect methods for estimating leaf area density and leaf area index of individual trees. *Agric. For. Meteorol.* **2020**, *292–293*, 108101. [CrossRef]
88. Le Saint, T.; Nabucet, J.; Sulmon, C.; Pellen, J.; Adeline, K.; Hubert-Moy, L. A spatio-temporal dataset for ecophysiological monitoring of urban trees. *Data Brief* **2024**, *57*, 111010. [CrossRef]
89. OpenStreetMap Contributors. Planet Dump. 2017. Available online: https://planet.osm.org (accessed on 1 September 2024).
90. Adeline, K.R.M.; Briottet, X.; Lefebvre, S.; Rivière, N.; Gastellu-Etchegorry, J.-P.; Vinatier, F. Impact of Tree Crown Transmittance on Surface Reflectance Retrieval in the Shade for High Spatial Resolution Imaging Spectroscopy: A Simulation Analysis Based on Tree Modeling Scenarios. *Remote Sens.* **2021**, *13*, 931. [CrossRef]
91. Widlowski, J.-L.; Côté, J.-F.; Béland, M. Abstract tree crowns in 3D radiative transfer models: Impact on simulated open-canopy reflectances. *Remote Sens. Environ.* **2014**, *142*, 155–175. [CrossRef]

92. Malenovský, Z.; Martin, E.; Homolová, L.; Gastellu-Etchegorry, J.-P.; Zurita-Milla, R.; Schaepman, M.E.; Pokorný, R.; Clevers, J.G.P.W.; Cudlín, P. Influence of woody elements of a Norway spruce canopy on nadir reflectance simulated by the DART model at very high spatial resolution. *Remote Sens. Environ.* **2008**, *112*, 1–18. [CrossRef]
93. Ichinose, M.; Inoue, T.; Nagahama, T. Effect of retro-reflecting transparent window on anthropogenic urban heat balance. *Energy Build.* **2017**, *157*, 157–165. [CrossRef]
94. Yang, Y.; Chen, Y.; Yang, K.; Cermak, J.; Chen, Y. High-resolution aerosol retrieval over urban areas using sentinel-2 data. *Atmospheric Res.* **2021**, *264*, 105829. [CrossRef]
95. Demuzere, M.; Kittner, J.; Bechtel, B. LCZ Generator: A Web Application to Create Local Climate Zone Maps. *Front. Environ. Sci.* **2021**, *9*, 637445. [CrossRef]
96. de Sá, N.C.; Baratchi, M.; Hauser, L.T.; van Bodegom, P. Exploring the Impact of Noise on Hybrid Inversion of PROSAIL RTM on Sentinel-2 Data. *Remote Sens.* **2021**, *13*, 648. [CrossRef]
97. Houborg, R.; Anderson, M.; Daughtry, C. Utility of an image-based canopy reflectance modeling tool for remote estimation of LAI and leaf chlorophyll content at the field scale. *Remote Sens. Environ.* **2009**, *113*, 259–274. [CrossRef]
98. Melendo-Vega, J.R.; Martín, M.P.; Pacheco-Labrador, J.; González-Cascón, R.; Moreno, G.; Pérez, F.; Migliavacca, M.; García, M.; North, P.; Riaño, D. Improving the Performance of 3-D Radiative Transfer Model FLIGHT to Simulate Optical Properties of a Tree-Grass Ecosystem. *Remote Sens.* **2018**, *10*, 2061. [CrossRef]
99. Verrelst, J.; Vicent, J.; Rivera-Caicedo, J.P.; Lumbierres, M.; Morcillo-Pallarés, P.; Moreno, J. Global Sensitivity Analysis of Leaf-Canopy-Atmosphere RTMs: Implications for Biophysical Variables Retrieval from Top-of-Atmosphere Radiance Data. *Remote Sens.* **2019**, *11*, 1923. [CrossRef]
100. Niu, C.; Phinn, S.; Roelfsema, C. Global Sensitivity Analysis for Canopy Reflectance and Vegetation Indices of Mangroves. *Remote Sens.* **2021**, *13*, 2617. [CrossRef]
101. Brede, B.; Verrelst, J.; Gastellu-Etchegorry, J.-P.; Clevers, J.G.P.W.; Goudzwaard, L.; den Ouden, J.; Verbesselt, J.; Herold, M. Assessment of Workflow Feature Selection on Forest LAI Prediction with Sentinel-2A MSI, Landsat 7 ETM+ and Landsat 8 OLI. *Remote Sens.* **2020**, *12*, 915. [CrossRef]
102. Malenovský, Z.; Homolová, L.; Lukeš, P.; Buddenbaum, H.; Verrelst, J.; Alonso, L.; Schaepman, M.E.; Lauret, N.; Gastellu-Etchegorry, J.-P. Variability and Uncertainty Challenges in Scaling Imaging Spectroscopy Retrievals and Validations from Leaves Up to Vegetation Canopies. *Surv. Geophys.* **2019**, *40*, 631–656. [CrossRef] [PubMed]
103. Ye, S.; Pontius, R.G., Jr.; Rakshit, R. A review of accuracy assessment for object-based image analysis: From per-pixel to per-polygon approaches. *ISPRS J. Photogramm. Remote Sens.* **2018**, *141*, 137–147. [CrossRef]
104. Liu, S.; Brandt, M.; Nord-Larsen, T.; Chave, J.; Reiner, F.; Lang, N.; Tong, X.; Ciais, P.; Igel, C.; Pascual, A.; et al. The overlooked contribution of trees outside forests to tree cover and woody biomass across Europe. *Sci. Adv.* **2023**, *9*, eadh4097. [CrossRef] [PubMed]
105. Tolan, J.; Yang, H.-I.; Nosarzewski, B.; Couairon, G.; Vo, H.V.; Brandt, J.; Spore, J.; Majumdar, S.; Haziza, D.; Vamaraju, J.; et al. Very high resolution canopy height maps from RGB imagery using self-supervised vision transformer and convolutional decoder trained on aerial lidar. *Remote Sens. Environ.* **2024**, *300*, 113888. [CrossRef]
106. Conrad, O.; Bechtel, B.; Bock, M.; Dietrich, H.; Fischer, E.; Gerlitz, L.; Wehberg, J.; Wichmann, V.; Böhner, J. System for Automated Geoscientific Analyses (SAGA) v. 2.1.4. *Geosci. Model Dev.* **2015**, *8*, 1991–2007. [CrossRef]
107. Le Saint, T.; Lefebvre, S.; Hubert-Moy, L.; Nabucet, J.; Adeline, K. Sensitivity Analysis of Sentinel-2 Data for Urban Tree Characterization Using DART Model. In Proceedings of the Remote Sensing Technologies and Applications in Urban Environments VIII, Amsterdam, The Netherlands, 3–4 September 2023; Erbertseder, T., Chrysoulakis, N., Zhang, Y., Eds.; SPIE: Bellingham, WA, USA, 2023; Volume 12735, p. 127350H.
108. Atmospheric Administration, United States Air Force. *US Standard Atmosphere*; National Oceanic and Atmospheric Administration: Washington, DC, USA, 1976.
109. Yu, K.; Van Geel, M.; Ceulemans, T.; Geerts, W.; Ramos, M.M.; Sousa, N.; Castro, P.M.L.; Kastendeuch, P.; Najjar, G.; Ameglio, T.; et al. Foliar optical traits indicate that sealed planting conditions negatively affect urban tree health. *Ecol. Indic.* **2018**, *95*, 895–906. [CrossRef]
110. Chianucci, F.; Pisek, J.; Raabe, K.; Marchino, L.; Ferrara, C.; Corona, P. A dataset of leaf inclination angles for temperate and boreal broadleaf woody species. *Ann. For. Sci.* **2018**, *75*, 50. [CrossRef]